The Surface Science Approach Toward Understanding Automotive Exhaust Conversion Catalysis at the Atomic Level

BERNARD E. NIEUWENHUYS

Leiden Institute of Chemistry, Gorlaeus Laboratories Leiden University
2300 RA Leiden, The Netherlands

This review focuses on the reactions and catalysts used for control of emissions of exhaust gases for gasoline-fueled automobiles with emphasis on fundamental understanding of the surface processes. Attention is paid to three-way catalysts, which simultaneously enhance the conversion of CO, hydrocarbons, and nitrogen oxides. The mechanisms of the CO oxidation and nitrogen oxide reactions, the specific differences in behavior of Pt, Pd, and Rh, the effect of alloy formation, and the role of ceria used as additive in three-way catalysts are discussed. Results of surface science studies are compared with results reported for supported catalysts. For CO oxidation, there is excellent agreement between results obtained for single crystal surfaces and supported catalysts. The kinetics of the reactions on pure metals can be understood on the basis of the kinetics parameters obtained from single-crystal studies. For the NO reduction reactions, there is qualitative agreement between results obtained with single-crystal and supported catalysts. The major effects of alloy formation can be understood on the basis of the surface composition.

Abbreviations: AES, Auger electron spectroscopy; E_{des}, activation energy for desorption; ESDIAD, electron-stimulated desorption ion angular dependence; hc, hydrocarbon; HREELS, high-resolution electron energy loss spectroscopy; L–H, Langmuir–Hinshelwood; LEED, low-energy electron diffraction; RAIRS, reflection absorption infrared spectroscopy; SERS, surface-enhanced Raman spectroscopy; SIMS, secondary ion mass spectrometry; TDS, thermal desorption spectroscopy, spectrum, or spectra; TPR(S), temperature-programmed reaction (spectroscopy); TOF, turnover frequency; TWC, three-way catalyst or catalysis; uhv, ultrahigh vacuum; UPS, UV photoelectron spectroscopy; XPS, X-ray photoelectron spectroscopy.

I. Introduction

Severe emission limits for motor vehicles were introduced, first in the United States and later in many other countries, starting in the mid-1960s. Meeting the increasingly stringent emission requirements in subsequent years forced the installation in motor vehicles of progressively more advanced emission control devices. The focal point of emission control is the catalytic converter, in which the desired chemical reactions occur. The pollutants carbon monoxide and unburned hydrocarbons (hc) are converted by oxidation into the desired CO_2 and water:

$$2CO + O_2 \rightarrow 2CO_2 \tag{1}$$

$$aC_nH_m + bO_2 \rightarrow cCO_2 + dH_2O, \tag{2}$$

and the pollutant nitrogen oxides are reduced to dinitrogen and CO_2 or H_2O:

$$2NO + 2CO \rightarrow N_2 + 2CO_2$$

$$2NO + H_2 \rightarrow N_2 + H_2O$$

$$aNO + bhc \rightarrow cN_2O + dCO_2 + eH_2O. \tag{3}$$

The first generation of automotive catalysts catalyzed only the two oxidation reactions (Eqs. 1 and 2) and, hence, these are called *two-way* catalysts. At that time much knowledge was available concerning oxidation catalysis, and it was relatively easy to develop the first automotive catalyst. Both noble metal and transition metal oxides were available to oxidize the CO and hc. Many transition metal oxides exhibit good catalytic properties for the oxidation reactions. However, the noble metals have superior properties with significantly lower light-off temperatures (the light-off temperature is the minimum temperature needed to start the reaction) and with better resistance to poisoning by sulfur compounds and other compounds present in the fuel or lubricant. The noble metals Pt and/or Pd were the active components of these catalysts. Small noble metal particles were supported by γ-alumina with high surface area and good thermal stability.

A new generation of catalysts was needed when the exhaust emission regulations in the United States changed, requiring lower levels for NO_x. After many years of research, it was determined that the most effective technology is a three-way catalyst (TWC) system, which simultaneously accelerates the NO_x reduction reactions and the oxidation of CO and hydrocarbons. The principle of TWC is illustrated in Fig. 1, which shows the change of the conversion of the three major pollutants as a function of the air/fuel ratio. The air/fuel ratio is usually expressed as the weight
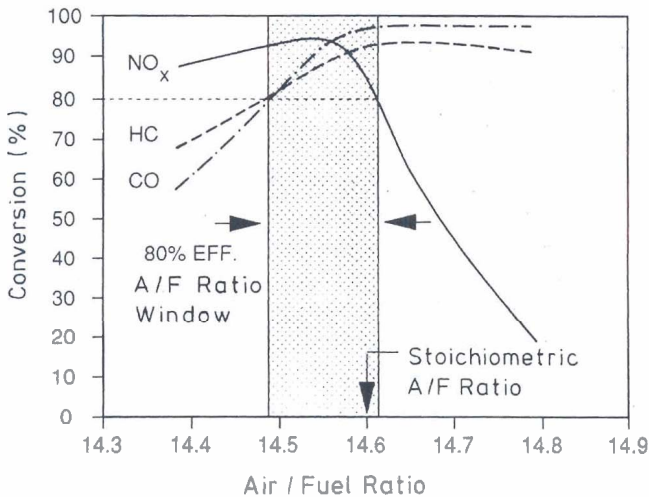
FIG. 1.   Efficiency of a three-way catalyst for the conversions of CO, NO, and hydrocarbons at various A/F ratios.

of air per weight of fuel. It is easily convertable into the equivalence ratio (λ), the value of which is unity at the stoichiometric point when all the fuel is completely converted to CO_2 and water. Obviously, the oxidation reactions (Eqs. 1 and 2) are favored under conditions of excess air ($\lambda > 1$), whereas complete reduction of nitrogen oxides requires reducing conditions ($\lambda < 1$). Fortunately, simultaneous conversion of NO, CO, and hc can occur in a narrow window around the stoichiometric composition $\lambda = 1$, as demonstrated in Fig. 1. Precise control of the air/fuel ratio is required to achieve high conversions of CO, hc, and NO. The composition of the air/fuel mixture introduced to the engine is electronically controlled by a feedback system with an oxygen sensor to monitor the oxygen concentration in the exhaust.

Most of the current converters consist of a flow-through ceramic monolith with its channel walls covered with a high-surface-area γ-Al_2O_3 layer (the washcoat) which contains the active catalyst particles. The monolith is composed of cordierite, a mineral with the composition $2MgO \cdot 2Al_2O_3 \cdot 5SiO_2$. The chemical composition of a modern TWC is quite complex. In addition to alumina, the washcoat contains up to 30 wt% base metal oxide additives, added for many purposes. The most common additives are ceria and lanthana; in many formulations BaO and ZrO_2 are used, and in some converters NiO is present. The major active constituents of the washcoat are the noble metals Pt, Pd, and Rh (typically 1–3 g). Most of the TWC systems in use today are still based on Pt and Rh in a ratio of about 10:1.

In the past 5 years, some of the Pt–Rh TWC formulations have been replaced by Pd-based TWC (the "Pd-only" TWC and Pd–Rh-based TWC), particularly in the United States.

In the past 30 years, automotive catalysis has become the greatest novel application of heterogeneous catalysis in the world. Automotive catalysis is a major application for the precious metals, as illustrated in Table I, which shows that the relative importance of Pt, Pd, and Rh for automotive catalysis changed considerably in the past decade. The current usage of Pd for automotive catalysis exceeds that of Pt. However, the Pd-based converters contain more precious metal than the Pt-based converters.

Many reviews (1–4) give detailed descriptions of the fundamentals of automotive exhaust catalysis. Shelef and Graham (3) gave a broad view of the unique properties of Rh in automotive three-way catalysis. This chapter focuses on fundamental processes taking place at the catalyst surface. Attention is given to the adsorption of the relevant gases, mechanisms of the relevant reactions, specific differences in the surface properties of the various noble metals, effects of alloy formation, and the chemistry of the additives, in particular ceria. The chemistry of the reactions shown in Eqs. (1)–(3) is understood in considerable detail as a result of recent studies using models of the TWC and surface science techniques. Relevant literature of diesel and lean exhaust gas control is also briefly discussed.

It is not the aim of this chapter to review all the available data. The data mentioned and the papers cited here are presented only to the extent that the findings illuminate the discussion.

TABLE I
Western World Demand for Pt, Pd, and Rh[a]

Metal	Year	$10^{-6} \times$ total demand, g	$10^{-6} \times$ automobile catalyst demand (gross), g	Percentage of total for automobile catalysts
Pt	1987	96	39	40
	1992	119	48	40
	1996	152	57	37
Pd	1987	98	8.4	8
	1992	121	15.2	13
	1996	212	72	34
Rh	1987	9.7	7.0	72
	1992	11.8	9.5	81
	1996	14.8	12.9	87

[a] Data from Platinum 1997 (Johnson Matthey).

II. Adsorption

A. ADSORPTION OF CO, HYDROGEN, OXYGEN, AND NO

The adsorption of diatomic molecules on a metal surface may be considered as competition between molecular and dissociative adsorption:

$$AB_{gas} \rightarrow AB_{ads} \rightarrow A_{ads} + B_{ads}. \tag{4}$$

Dissociative adsorption can occur when the bonds formed between the fragments of the dissociated molecule and the surface are much stronger than the bonds between the molecule and the surface. For example, molecular hydrogen, oxygen, or nitrogen is only weakly adsorbed on transition metals. Oxygen, hydrogen, and nitrogen adatoms, on the other hand, are strongly bound on many metal surfaces. Therefore, dissociative adsorption is often thermodynamically possible, as discussed later. Molecular adsorption of CO and of NO is relatively strong on many metal surfaces. These adsorbates may undergo both dissociative and molecular adsorption on the same surface depending on the experimental conditions.

It is often observed that molecular adsorption prevails at lower temperatures and that dissociative adsorption occurs at higher temperature. This pattern may be caused by kinetics; the activation energy for dissociative adsorption is too high for dissociation at lower temperatures. There may also be a thermodynamic reason. If the number of surface sites at which adsorption can take place is equal for molecular and dissociative adsorption, the surface can accommodate twice as many molecules in the molecular state as it can in the dissociated state. Hence, molecular adsorption will prevail if the heat of dissociative adsorption is not much greater than the heat of molecular adsorption. The entropy change for adsorption is negative and, consequently, at sufficiently high temperatures desorption will occur. In the case considered previously, only half the number of molecules can be adsorbed in the dissociative state as can be adsorbed in the molecular state. As a result, the entropy of the system will be lower for molecular adsorption and dissociation can occur at higher temperatures.

Dissociative adsorption requires a cluster of several free and adjacent metal atoms on the surface. Therefore, often dissociation occurs when the surface coverage is low and molecular adsorption occurs above a certain coverage, provided that both dissociative and molecular adsorption can occur under the experimental conditions considered.

It is assumed that a diatomic molecule adsorbed parallel to the surface is in a transition state for dissociation. The more favorable adsorption complex for molecules such as CO on a group VIIII metal surface is that in which the molecular axis is bonded perpendicular to the surface (or

slightly tilted). It has been demonstrated by electron-stimulated desorption ion angular distribution (ESDIAD) that the molecular axis vibrates around the surface normal and that its amplitude increases with increasing temperatures (5) (Fig. 2). The temperature at which dissociation occurs is probably reached when the vibrational amplitude becomes sufficiently large so that a bond between the O atom and the metal surface is formed, resulting in dissociation.

Many of the adsorption data presented in this review are based on thermal desorption spectroscopy (TDS) measurements. This technique yields in a simple way information about the number of binding states and their bond strengths with the surface. For illustration, TD spectra are shown for molecules adsorbed on a Rh filament.

TDS measured for polycrystalline surfaces are often much more complicated than those representing single-crystal surfaces. A polycrystalline surface exhibits all the adsorption sites of the crystal faces of which it is composed. Since these sites are simultaneously present, a TDS represents an average of the spectra of the different surface sites weighted according to the relative concentrations of these sites.

⊥. *Adsorption of Hydrogen*

Hydrogen is known to be dissociatively adsorbed on transition metal surfaces, and the initial sticking probability varies from about 0.05 to unity at $T = 100-300$ K, depending on the metal and its surface structure. For example, the initial sticking probability for hydrogen on a Ni(111) surface is only 0.05; on the stepped Ni-8(111) $\times$ (100) surface it is 0.2, and on a Ni(110) surface it is essentially unity (6). In general, the sticking probability is significantly smaller on flat surfaces than on surfaces with high densities of steps, surface defects, etc. It appears that hydrogen prefers to be adsorbed on sites on which it is coordinated with many metal atoms. On (111) surfaces
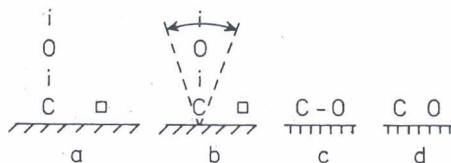

FIG. 2. Molecules such as CO are bonded on most of the group VIII metal surfaces with the molecular axis perpendicular to the surface (a) or slightly tilted. The amplitude of the vibration around the surface normal increases with increasing temperature (b). At a certain temperature, an O–metal bond is formed (c) and dissociation occurs immediately (d).

of the face-centered cubic (FCC) lattice, for example, hydrogen is adsorbed at low coverage on threefold sites. Hydrogen desorbs from the group VIII metals at about 350–400 K; its initial heat of adsorption lies in the range 80–100 kJ mol^{-1} and is the same within 20% on similar surfaces of these metals. More details are given in Nieuwenhuys (7).

2. Adsorption of Oxygen

The interaction of oxygen with Pt surfaces has been studied in detail with modern surface analytical techniques (7). Since the TDS of oxygen on most of the other metals of group VIII are qualitatively similar to those for oxygen on Pt, one can expect that essentially the same species occurs on all these metals. At 100 K, oxygen is adsorbed on Pt(111) with a sticking probability of about unity in a molecularly adsorbed state (γ state) with a low heat of adsorption (37 kJ/mol) (8). Electron energy loss spectroscopy (EELS) combined with UV photoelectron spectroscopy (UPS) indicates an essentially single O–O bond with a significant electron transfer from the valence band of Pt into orbitals derived from the π antibonding oxygen levels and with the O–O bond axis parallel to the surface. Heating the surface to temperature above 170 K results in the formation of adsorbed atomic oxygen (β–O) and desorption of some oxygen (γ). The heat of adsorption of β–O decreases rapidly with increasing coverage from 500 to 160 kJ/mol at $\theta = 0.8\ \theta_{max}$. On Pt(111) surfaces, oxygen is adsorbed at 300 K with a low sticking probability (<0.1).

A third state is sometimes observed upon heating Pt(111) in the presence of oxygen in the 900 K temperature range (8). This subsurface oxygen, which desorbs at temperatures higher than 1200 K, has a very low reactivity toward CO and hydrogen. There is controversy concerning the nature of this state (7). Many authors believe that this state is a so-called surface oxide (Fig. 3), whereas others attribute its appearance
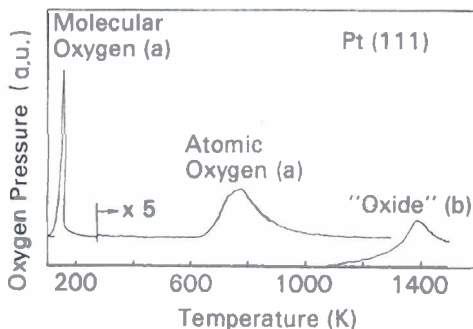

FIG. 3.   TDS of oxygen from Pt(111) [reproduced with permission from Gland et al. (8)].

to oxide-forming bulk impurities such as Si or Ca and its segregation to the surface during oxygen exposure at high temperature. On polycrystalline surfaces and on open surfaces, the formation of an oxide layer at higher temperature is quite common as is demonstrated by field emission microscopy (7).

In contrast to adsorbed CO, the density of O adatoms at saturation is not determined by the size of the adsorbate; more open overlayer structures are usually formed. The kinetics of oxygen adsorption at ambient temperature varies greatly from metal to metal and from plane to plane. For example, oxygen is adsorbed with a sticking probability near unity on Ni surfaces, whereas on Pt(111) the sticking probability is <0.1. The initial heat of adsorption of β–O is approximately 250 kJ/mol on the group VIII metals, corresponding to a metal–O bond strength of about 370 kJ/mol. Because of the high desorption temperature, the appreciable decrease of the heat of adsorption Q with increasing coverage, and the incorporation of oxygen into the bulk, it is not easy to find a correlation of $Q_{initial}$ with the position of the metal in the periodic table. A careful examination of reliable data suggests that the heat of adsorption increases in the following order: Pt (230 kJ/mol) = Pd < Ir < Rh < Ru < Ni (330 kJ/mol). The variation in the metal–O bond strength is about 55 kJ/mol (or 15%). The order in the heat of adsorption is similar to that in the heat of formation of the oxides. The tendency of the metal to form surface or bulk oxides also increases in this sequence. It can be concluded that, in contrast to hydrogen on group VIII metals, there are significant differences in the metal–O bond strength on these metals.

3. Adsorption of CO

CO on metals is the most extensively studied adsorption system (9). I highlight some of the features that are important for this discussion. TDS of CO on group VIII metal surfaces in general show various peaks, which can be classified into three main groups as shown schematically for CO on polycrystalline Rh in Fig. 4 and corresponding to the following:

1. Low-T γ states desorbing at temperatures much lower then room temperature,

2. α states with a peak maximum in its TDS between 350 and 500 K.

3. Sometimes, depending on the choice of the metal, its surface structure, and the experimental conditions (such as the temperature), additional states (β) are observed with a maximum of approximately 900 K. These β states arise from CO dissociation followed by recombination of C and O at the desorption temperature.
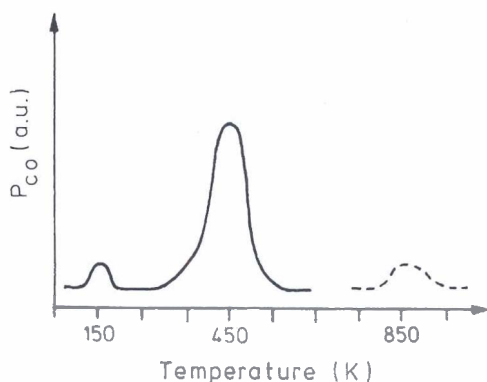
FIG. 4.   TDS of CO from Rh [reproduced with permission from Nieuwenhuys (7)].

At room temperature, adsorption normally takes place in the α state corresponding to molecularly adsorbed CO. Usually two or more α peaks are observed, depending on the surface structure and the CO coverage. These peaks can be rationalized on the basis of distinct species adsorbed on different sites and in terms of lateral interactions.

A model of the α–CO metal bond was first proposed by Blyholder (10). According to this model, the bond is formed by electron transfer from the highest filled molecular orbital of CO (5σ, which is essentially a nonbonding orbital with respect to the C–O bond) to unoccupied metal orbitals, implying a donation of electrons to the metal, accompanied by back-donation of electrons from occupied d orbitals into the lowest unfilled CO molecular orbital (the strongly antibonding 2π orbital). The relative contributions of the σ and the π bonding to the metal–CO bond strength and to the net charge transfer have been discussed in many papers. Sufficient evidence, based on theoretical calculations (11, 12) and inverse photoemission studies (13), indicates that for Pd and Ni metal, π donation to CO is much more important for the CO–metal bond than is the CO-to-metal σ donation. However, the CO–Pt bond has a significant σ-donation component (13). Furthermore, work function measurements indicate that the net electron transfer from metal to CO is much larger for Rh, Pd, and Ni than for Pt (14).

Experimental and theoretical results support the fact that the CO molecules are adsorbed on the densely packed surfaces of Pt, Pd, Rh, and Ir with the C–O axis normal to the surface and with the carbon atom directed to the surface. Experimental evidence is derived from angular resolved UPS, ESDIAD, ion scattering, low-energy electron diffraction (LEED) intensity analysis, and EELS.

LEED, IR, or EELS and TDS have been applied for CO on many single-

crystal surfaces. The general features of these are very similar. First, a simple overlayer structure is formed up to medium coverage. For example, on the FCC(111) surfaces, $(\sqrt{3} \times \sqrt{3})R30°$ structures are observed which are fully developed at $\theta = 1/3$. The molecules are then located on most of the densely packed surfaces in identical sites. At higher coverage, the overlayer unit cell is compressed, new surface structures are observed, and a fraction of the CO molecules are forced to move into other sites. At the highest coverage, a close-packed overlayer is formed which is largely determined by the CO–CO mutual repulsion and not by the substrate sites. The maximum density of adsorbed CO molecules is about 1×10^{15} molecules/cm². The sites on which CO molecules are bound are reflected in the stretching vibration frequencies ν of the CO bond. In the pioneering work of Eischens *et al.* (*15*), bands at frequencies below 2000 cm^{-1} were assigned to CO acting as a bridging ligand, $M_2C{=}O$, and bands between 2000 and 2100 cm^{-1} were attributed to linear CO species such as $M{=}C{=}O$. Numerous results have shown that Eischens *et al's*. interpretation of the bands was essentially correct, and more comprehensive correlations of ν with bonding sites have been suggested (*16*).

A substantial increase in ν occurs with increasing surface coverage. Both experimental observations, based on the combined use of TDS, LEED, and EELS/IR, and theoretical predictions suggest that the energy difference of CO bonded in on-top positions or in multifold sites is quite small. The only metal on which bridged (or multifold) sites are the most favorable positions for CO is Pd. On Ir, Rh, and Ru, linearly adsorbed CO is preferred. Also, on Pt(111) on-top positions are preferred, but the energy differences with the other positions are small, resulting in a high degree of disorder at room temperature, as observed by LEED (*7*). The differences in heat of adsorption on the group VIII metals for the various single-crystal surfaces of a metal are about 20 kJ/mol (or 20%) (*7*).

Dissociative adsorption of CO has been found on a variety of transition metal surfaces. Broden *et al.* (*17*) and Nieuwenhuys (*14*) correlated the tendency for CO, N_2, and NO to dissociate with the position of the transition metal in the periodic table; the tendency for dissociation increases the further to the left the metal appears in the table, and it decreases from 3d to 5d metals. Furthermore, the borderline for dissociative or molecular adsorption moves to the right in the sequence CO, N_2, NO to O_2, being the same order as the bond strength in the free molecules. There is sufficient evidence for the proposed correlation. For example, W and Mo surfaces dissociate CO easily at room temperature; dissociative adsorption has not been reported for Pt, Ir, and Pd(111) surfaces, and CO dissociation has been reported to occur on Ni, Co, and Ru at elevated temperatures. Benzinger (*18*) suggested that the state of adsorption (molecular or dissociative)

is determined by thermodynamic criteria. In his paper, the heat of dissociative adsorption was estimated from the heats of formation of metal carbides, nitrides, and oxides. In this analysis, a similar correlation as that in Refs. (14) and (17) relating dissociative adsorption with position in the periodic table was found. The surface structure may have an additional influence on the dissociation. In general, close-packed surfaces are the least reactive and rough surfaces or surfaces with steps or kinks are the most reactive for dissociation. The effect of surface structure on dissociation can be attributed to the variation of, e.g., metal–carbon bond strength with surface structure.

For our purposes, it is relevant to conclude that CO adsorption is predominantly molecular on Pt, Ir, Pd, and Rh and that desorption occurs at about 500 K. Controversy exists in the literature regarding CO dissociation on Rh surfaces (19). On supported Rh catalysts and Rh clusters, CO dissociation has been observed. Some authors also reported CO dissociation on certain single-crystal surfaces, whereas other studies indicate no or insignificant dissociation on clean Rh surfaces (19).

4. *Adsorption of NO*

Figure 5 presents a TD spectrum for NO adsorbed on a Rh filament at 80 K (20), showing desorption peaks of NO, N_2, and O_2. The heat of
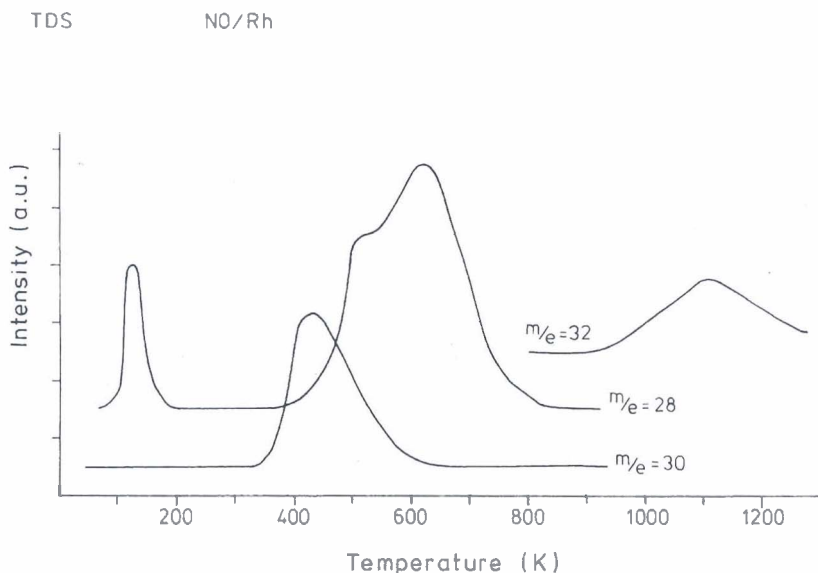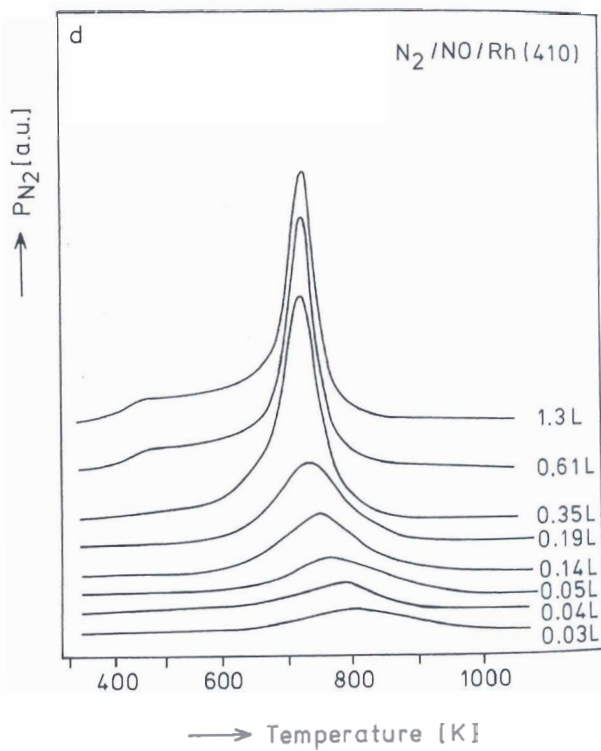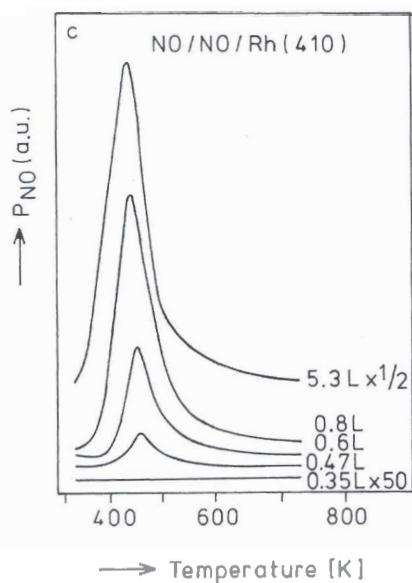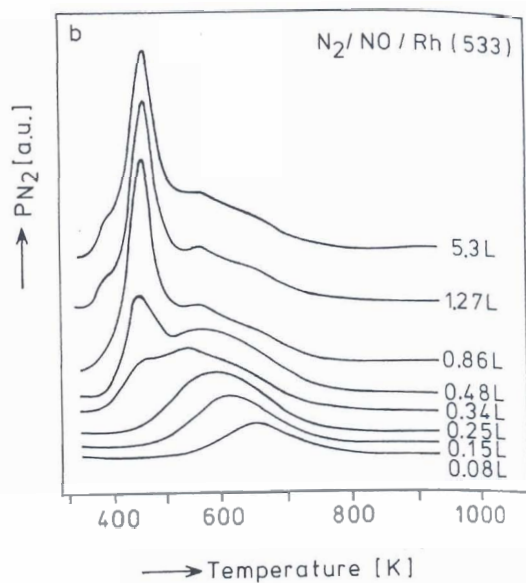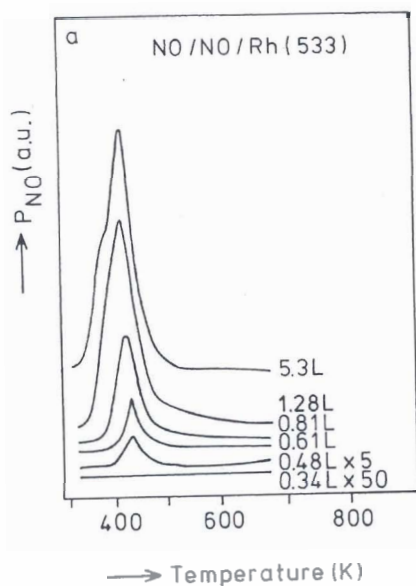

FIG. 5.   TDS of NO, N_2, and O_2 following adsorption of NO on a Rh filament at 80 K [reproduced with permission from Hendrickx and Nieuwenhuys (20)].

adsorption of molecularly adsorbed NO is on the order of 110 kJ/mol^{-1} for the group VIII metals. The energy barrier for dissociation is much lower for NO than for CO due to the presence of one electron in the antibonding 2π orbital. The temperature at which dissociation starts depends strongly on the NO coverage and is very sensitive to the surface structure. For example, when a NO-covered Rh(331) surface is heated, dissociation starts even at 240 K for a low NO coverage (21). However, a temperature of 350 K is required for a surface that starts fully covered. These results show that some of the molecularly adsorbed NO must desorb in order to create free sites needed for dissociation. Van Hardeveld (22) investigated the adsorption of NO on Rh(111) with secondary ion mass spectrometry (SIMS); a technique that measures the composition of the adsorbate layer and TDS. At temperatures higher than 250 K, a substantial fraction of the NO dissociates during adsorption. At temperature higher than 350 K NO$_{ads}$ is absent; the dissociation is complete. The decrease of the dissociation rate with increasing coverage can be explained by assuming that an ensemble of three or four empty sites is required for NO dissociation (23). The authors argued that a more likely explanation is that lateral interactions between NO$_{ads}$ and O$_{ads}$ or N$_{ads}$ cause the decrease in dissociation rate with increasing coverage.

EELS spectra (7) for NO on Ru(001) at temperatures higher than 180 K are consistent with a model in which NO is adsorbed in bridged or threefold sites (state α_1, $\nu_{NO} = 1500$ cm^{-1}), and in on-top sites (state α_2, $\nu_{NO} = 1800$ cm^{-1}). At low coverage, NO is adsorbed in the more strongly bound α_1 state and, at coverages $>1/3$ of saturation, the on-top sites become populated. Exposure at 280 K causes dissociation of α_1 NO. ESDIAD studies suggest that the N–O bond is predominantly normal to the surface in both molecular states. Ku et al. (For ref. see (7)) concluded from LEED observations following NO dissociation on a Ru(1010) surface that the N and O adatoms form separate islands on this surface. Many investigations indicate that molecularly adsorbed NO is highly inclined at low coverage, whereas at high coverage, this adsorbate has a perpendicular orientation. Examples are NO on Ni(111), Ni(100), Pt(100), and Rh(100) (24). The tilted species is usually considered to be a precursor for dissociation.

Somorjai (25), Gorte et al. (26), and Masel (27) found that NO dissociation is neglegible on perfect Pt(111) surfaces. Surface defects bind NO

FIG. 6.   TDS of NO on Rh(533) and (410) surfaces. (a) NO from (533), (b) N$_2$ from (533), (c) NO from (410), and (d) N$_2$ from (410), Heating rate = 20 Ks^{-1} [reproduced with permission from Janssen et al. (28)].

more tightly on Pt and induce dissociation. Gorte *et al.* reported that the Pt(100) surface has stronger bonding and much higher decomposition activity than the Pt(110) and (111) surfaces. The major tightly bound state on Pt(100) dissociates to yield 50% N_2 and O_2, whereas the fraction decomposed on the Pt(111) surface is <2%. The stepped Pt(410) surface with (100) terraces is much more reactive in NO dissociation than the (100) surface (*27*). On Pd(111), the rate of NO dissociation becomes significant at temperatures higher than 500 K (*7*). In addition to desorption of NO, N_2, and O_2, production of N_2O has been observed on many Pd and Pt surfaces.

On Rh surfaces, only desorption of N_2 and NO is observed in the TDS. Figure 6 shows TDS for NO on two stepped Rh surfaces, Rh(533) [structure 4(111) × (100)] and Rh(410) [structure 4(100) × (100)]. The adsorption of NO and the effect of preadsorbed O and N on the adsorption of NO have been studied on these surfaces and on many other Rh surfaces by Janssen *et al.* (*28*). The N atoms are markedly more strongly bound on (100) terraces than on (111) terraces. The presence of steps does not affect the thermal stability of N_{ads} on Rh. At higher NO exposures, repulsive N–N and N–O interactions lower the thermal stability of N_{ads}. Following saturation NO exposure, N_2 desorbs in a single state from (100) terraces at 750 K. From (111) terraces several desorption states of nitrogen appear at temperaturs between 450 and 700 K. An important observation is that recombination of N_{ads} and O_{ads} to give NO is more favorable than the 2 $N_{ads} \rightarrow N_2$ reaction when Rh with precovered O_{ads} is exposed to NO.

The literature suggests that on Pd and Pt surfaces adsorption of NO is predominantly molecular at room temperature. Dissociation is observed at elevated temperatures, and the surface structure has a significant influence on the extent of dissociation. In contrast to the adsorption of CO, dissociation of NO can easily be detected on Ir, Rh, and Ru surfaces at room temperature.

B.   ADSORPTION OF N_2, H_2O, CO_2, N_2O, AND NH_3

Various techniques have been used to investigate the interaction of N_2, H_2O, CO_2, and NH_3 with clean metal surfaces. The adsorption of N_2O has not been studied in detail.

The interaction of CO_2 with group VIII metals was reviewed by Solymosi (*29*). At 80 K, the adsorption on a Rh field emitter exhibits an interesting crystal face dependency (*30*). In addition to molecular adsorption, dissociation occurs at an appreciable rate on the stepped surfaces around (111) and (100) at temperatures higher than 220 K. The field electron microscopy (FEM) patterns suggest that the surface structure of Rh has a striking influence on the ability of the metal to dissociate the CO_2 molecule. From

Pt, CO_2 desorbs at a much lower temperature (90 K, corresponding to a heat of adsorption of about 20 kJ/mol), and dissociation was not detected (*30*).

No evidence was found for significant dissociation of NH_3 on Pt(111) and Ru(001) under low-pressure conditions. However, decomposition of NH_3 occurs at temperatures higher than 600 K in a NH_3 atmosphere (*31*). The effect of the surface structure on the dissociation is large. For Pt the order in reactivity is $(210) > (110) > (100) > (111)$ (*31*).

In the temperature range 80–400 K, nitrogen is only molecularly adsorbed on the group VIII metal surfaces, with the exception of Fe and Co, on which slow dissociation is observed on some faces at temperatures higher than 300 K (*7*). The nature of the adsorption bond is similar to that of the CO–metal bond. The heat of adsorption, however, is significantly lower for N_2 (40 kJ/mol) than for CO (130 kJ/mol) on the same surfaces, as demonstrated by the data in Fig. 7. It can be concluded from the available data that N_2, H_2O, N_2O, and CO_2 molecules leave the surface immediately upon formation.

C. COADSORPTION

To understand the catalytic properties of the various group VIII metal surfaces, the interactions among neighboring adsorbed species and their
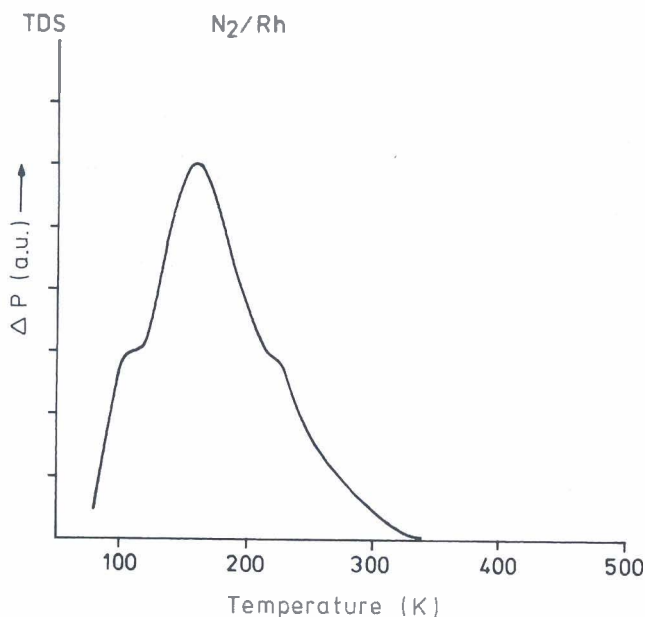

FIG. 7. TDS of nitrogen from a Rh filament [reproduced with permission from Nieuwenhuys (*7*)].

effects on the surface processes must be known since the surfaces may be covered with different kinds of adsorbates during the reaction.

Conrad *et al.* (*32*) studied in detail the mutual interaction of coadsorbed O and CO on a Pd(111) surface. Some of their relevant results are summarized here. Oxygen adsorption is inhibited by preadsorbed CO. At coverages below $\theta_{CO} = 1/3$, LEED patterns show that O and CO form separate surface domains. However, the behavior is different when O is preadsorbed. CO can be adsorbed on the Pd(111) surface covered with O which is less densely packed than a saturated CO layer. The O adatom islands are then suppressed to domains of a $(\sqrt{3} \times \sqrt{3})$R30° structure ($\theta = 1/3$), with a much larger local coverage than can be reached with O alone, which orders in a (2×2) structure ($\theta = 0.25$). After further exposure, the LEED patterns suggest the formation of mixed phases of O_{ads} and CO_{ads} (with local coverages of $\theta_O = \theta_{CO} = 0.5$) which are embedded in CO domains. When these mixed phases are present, CO_2 is produced even at temperature lower than room temperature. Coadsorption studies of other noble metal surfaces are consistent with this scenario; preadsorbed CO inhibits the dissociative adsorption of oxygen, whereas CO is adsorbed on a surface covered with O.

Lambert and Comrie (*33*) concluded from TDS on Pt(111) and (110) that gaseous CO displaces molecularly adsorbed NO (α_1) and also causes the conversion of this state to the other more weakly bound state α_2. The α_1 state was reported to be the only one which is reactive with CO. Displacement of molecularly adsorbed NO by gaseous CO has also been observed on Pd surfaces. Thiel *et al.* (*34*) used EELS to observe directly the competition of CO adsorption with one of the two molecular states of NO on Ru(001). The stretching frequencies suggest that (i) CO is linearly bonded to a single Ru atom, whereas NO prefers the bridging or multifold sites, and (ii) at higher coverages, linear sites are also populated. The EEL spectra indicate that conversion from linear to multifold bonded NO occurs during adsorption of CO. Similar observations have been made for CO–NO mixtures on Pd(110) (*35*). For each single-phase system, the bridge site is preferred. When the two are coadsorbed, however, a mixed phase is formed in which the stable CO site is linear. In the presence of a CO–NO atmosphere, Pt surfaces favor CO adsorption, as expected on the basis of the heats of adsorption (*36*). Rh surfaces, however, adsorb both CO and NO (*36*). Blocking of hydrogen adsorption by NO is observed on Rh surfaces (*21*). The occurrence of strong (repulsive or attractive) interactions between coadsorbed H and NO has not been reported.

In conclusion, the main effects found for coadsorption are blocking, island formation, displacement by the component with the higher heat of adsorption, and site conversion. Strong attractive interactions between the two adsorbates do not take place.

III.   CO–O$_2$ Reaction

Usually, temperatures of 300–600 K are required for the CO–O$_2$ reaction on the active metal catalysts Pt, Pd, Ir, Rh, Ru, and Ni. CO oxidation catalysts are used mainly for automotive emission control. In addition, air-purification devices for respiratory protection and CO gas sensors commonly employ CO oxidation catalysts. A novel application is in sealed CO$_2$ lasers used for weather monitoring and in other remote-sensing applications. For the development of long-life sealed CO$_2$ lasers, novel catalysts must be developed which are able to oxidize CO at temperatures near ambient. Active catalysts for this purpose are based on gold and a transition metal oxide, e.g., Au–manganese oxide (37). The mechanisms of the processes responsible for the high activity are not fully understood. In my opinion, the reaction may occur at the Au–MnO$_x$ interface with CO adsorbed on Au reacting with O on MnO$_x$. An alternative explanation is that O atoms spill over from MnO$_x$ to gold. Gold is not very active in O–O bond scission. However, O adatoms are stable on gold at room temperature. In the presence of CO, the O adatom can easily react with CO due to the low Au–O and Au–CO bond strengths.

Two mechanisms have been suggested for reactions such as oxidation of CO:

1. An Eley–Rideal mechanism in which one of the components reacts in the adsorbed state with the other molecule in the gaseous or in a physically adsorbed state, e.g.,

$$O_{ads} + CO_{gas} \rightarrow CO_2. \tag{5}$$
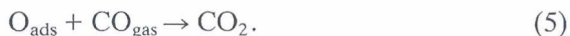
2. Langmuir–Hinshelwood mechanism in which both components react with each other in the adsorbed state, e.g.,

$$O_{ads} + CO_{ads} \rightarrow CO_2. \tag{6}$$

It has been established (38) that the dominant mechanism of the reaction is the Langmuir–Hinshelwood (L–H) mechanism:

$$CO \rightarrow CO_{ads} \tag{7}$$

$$O_2 \rightarrow 2O_{ads} \tag{8}$$

$$O_{ads} + CO_{ads} \rightarrow CO_2. \tag{9}$$

The alternative Eley–Rideal mechanism fails to explain all the experimental results. Direct evidence in favor of the L–H mechanism has been obtained

from molecular beam experiments. Figure 8 (*39*) shows a typical example of the variation in rate of CO_2 production with time for a CO beam impinging on an O adlayer on Pd(111) at a constant temperature of 374 K and also the variation of the surface concentrations of O_{ads} and CO_{ads}. The reaction exhibits an induction period and reaches its maximum rate after a few seconds. Obviously, the data of Fig. 8 confirm that both reactants must be adsorbed, in accordance with the L–H mechanism.

The reaction may thus be written as:

$$dp_{CO_2}/dt = k\theta_{CO}\theta_O = v\theta_{CO}\theta_O \exp[-E_a(\theta_{CO}, \theta_O)/RT], \qquad (10)$$

where θ_{CO} and θ_O are, respectively, the surface coverages by CO_{ads} and O_{ads}; E_a is the activation energy for the reaction, which may vary with θ_{CO} and θ_O; k is the rate constant and v the frequency factor. Both for Pd(111) and for Pt(111), E_a is equal to 101 kJ/mol at low-coverage of CO and O (*40*). A much lower value of the activation energy (50 kJ) was found when a Pt(111) surface saturated with O was exposed to a CO molecular beam. This decrease in E_a was attributed to a decrease in heats of adsorption of CO and O due to repulsive interactions.

At higher O coverages, deviations from Eq. (10) can be expected because
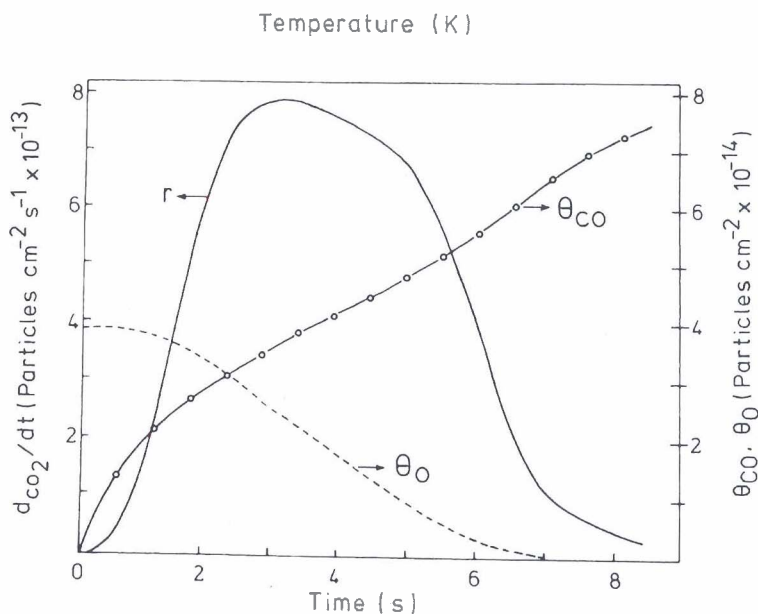

FIG. 8. Rates of CO_2 formation on Pd(111) and O and CO coverages as a function of time at 374 K [reproduced with permission from Engel and Ertl (*39*)].

the O atoms form islands on the surface due to attractive interactions (*41*). Sufficient evidence exists that the reaction proceeds at the boundaries of O and CO islands (*42*), under both low- and high-pressure conditions and on Pt single-crystal surfaces as well as supported catalysts (*43*).

Recently, very interesting results were reported by Wintterlin *et al.* (*44*). The reaction was imaged on Pt(111) by a variable-temperature scanning tunneling microscopy, (STM). Small O islands with (2×2) structure and, at high CO coverage, CO adatoms were resolved. The results show clear evidence of separate CO and O domains with the reaction taking place at the island boundaries. The activation energy for CO_2 formation found from these microscopic measurements was equal to the value reported by Campbell *et al.* (*40*) using macroscopic measurements.

Figure 9 shows the rate of CO_2 production catalyzed by the (111), (100), (410), and (210) surfaces of a $Pt_{0.25}$–$Rh_{0.75}$ single crystal as a function of temperature in the presence of a 2:1 mixture of CO and O_2 at a total pressure of 2×10^{-7} mbar (*45*). It shows that the reaction rate increases rapidly between 400 and 500 K to a temperature T_m at which a maximum is reached and beyond which it gradually decreases. The temperature at which the maximum occurs increases with increasing CO pressure. Similar behavior was found for many Pt, Pd, Ir, Rh, and Ru surfaces. X-ray photoelectron spectroscopy (XPS) measurements show that the maximum rate
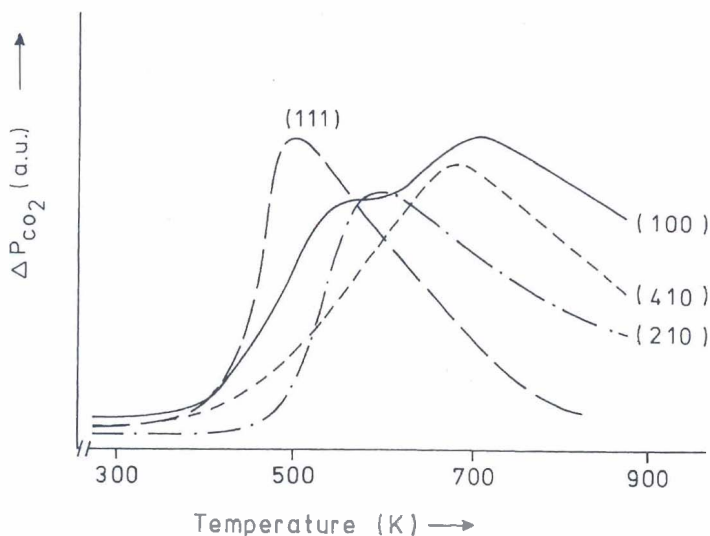

FIG. 9.   Steady-state rates of CO_2 production for the CO + O_2 reaction on the (111), (100), (410), and (210) surfaces of a $Pt_{0.25}$–$Rh_{0.75}$ single crystal [reproduced with permission from Siera *et al.* (*45*)].

is reached at a temperature at which the CO coverage is already small (7). These and other observations indicate that adsorbed CO acts as an inhibitor for O adsorption and, hence, for the catalytic reaction. The value of T_m is determined by the sticking probability, the enthalpy of adsorption of oxygen, and the enthalpy of adsorption of CO. The relatively small CO inhibition of the reaction on the (111) surface is consistent with the low heat of adsorption of CO on that surface.

Oscillations in the rate of CO_2 production have been observed for many supported metal catalysts and single-crystal surfaces. Similar oscillations have been observed for most of the reactions discussed in this review. An example is shown in Fig. 10 for the $NO + H_2$ reaction on Pt(100) (46).

Several models have been proposed to explain these oscillatory rates. Sales *et al.* (47) associated the oscillation with a slow and reversible modification of the catalyst surface; slow oxidation and reduction of the metal surface induces transitions between the two branches.

Ertl (38) reported in detail the oscillations on the (100) and (110) surfaces of Pt. The clean (100) and (110) surfaces reconstruct, i.e., the atomic arrangement in the topmost layer is not that of the corresponding bulk plane. However, the reconstruction is lifted by adsorption of CO and NO when
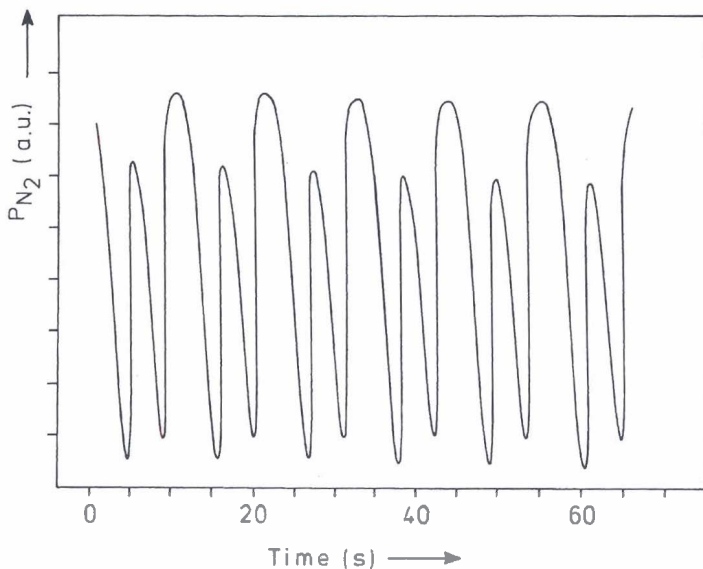

FIG. 10. Oscillatory behavior of the $NO + H_2$ reaction on Pt(100) [reproduced with permission from Cobden *et al.* (46)].

the coverage exceeds a certain critical value. The driving force is the higher heat of adsorption of CO on the nonreconstructed surface, which overcompensates the energy required for altering the surface structure. The sticking probability of oxygen is negligibly small on the reconstructed surface, whereas it is much higher on the nonreconstructed surface.

Ertl and coworkers (38) proposed the following model for oscillations: The surface structure changes to the nonreconstructed surface due to CO adsorption. Oxygen can then be adsorbed due to its relatively high sticking probability on this surface. The adsorbed O reacts with adsorbed CO molecules to yield CO_2 that is immediately released into the gas phase. As a result, more sites are created for oxygen adsorption and the reaction rate increases. The CO coverage decreases because of its rapid reaction with O. At the critical CO coverage, the surface structure transforms back into the reconstructed phase. Oxygen is not adsorbed anymore and, hence, the reaction rate decreases. The CO coverage then increases and, beyond the critical coverage, the surface structure transforms again to the nonreconstructed phase. This transformation completes the cycle of the oscillation. Recent studies suggest that rate oscillations under isothermal conditions can also occur on surfaces for which the reconstruction model does not apply. A more general model was proposed involving the key role of vacant sites on the surface required for dissociation of molecules such as NO and O_2 (48). For recent reviews concerning the oscillatory behavior of surface reactions, see Refs. (48, 49).

New regulations in the United States and Europe mandate that automotive emissions must decrease substantially from current levels. As a result, there is a strong incentive to develop improved TWC with better oxidation activity at low temperatures since most of the hydrocarbons and CO are emitted immediately following cold starts of engines. As previously mentioned, the addition of transition metal oxides can have a beneficial effect on the performance of Au catalysts in CO oxidation. Combinations of Pt or Pd with transition metal oxides are also active in CO oxidation at low temperatures (50). Figure 11 shows examples of the reaction over Pt/MO/SiO_2 catalysts.

Preoxidation does not significantly affect the temperature of 50% conversion ($T_{50\%}$) on Pt/SiO_2. Oxidation increases the $T_{50\%}$ on Pt/CoO_x/SiO_2. However, $T_{50\%}$ is still much lower for Pt/MO catalysts than for Pt/SiO_2. Similar effects were found for other CO/O_2 ratios. These experiments were continued for many hours. The $T_{50\%}$ of a Pt/CoO_x/SiO_2 catalyst shifts to a value between $T_{50\%}$ for the prereduced catalyst and the $T_{50\%}$ for the preoxidized catalyst, depending on the CO/O_2 ratio. Pt/CoO_x/SiO_2 is the most active of the catalysts investigated in our laboratory. At room temperature, CO is oxidized to CO_2. The value of $T_{50\%}$ are 100–200 K lower than those
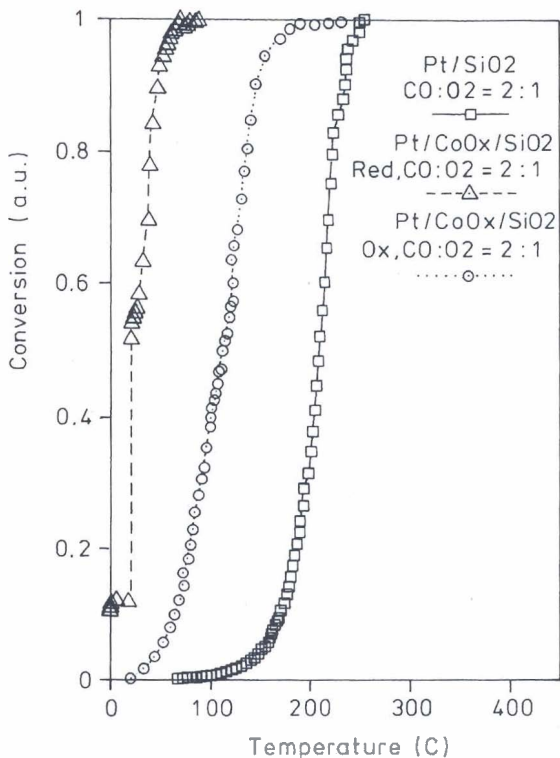
FIG. 11. CO conversion at various temperatures during CO oxidation with $CO:O_2 = 2:1$ catalyzed by Pt/SiO_2 and by $Pt/CoO_x/SiO_2$ after a reductive and an oxidative pretreatment [reproduced with permission from Mergler *et al.* (*50*)].

for Pt/SiO_2, depending on the CO/O_2 ratio. CoO_x/SiO_2 does not exhibit significant activity at temperatures below 498 K. The Pt/MO catalysts also exhibit improved performance in NO reduction reactions (*51–53*).

IR (*53*) and temporal analysis of products (TAP) (*54*) have been used to investigate the origin of the improved performance of the Pt/MO catalysts in CO oxidation. The TAP experiments shown in Fig. 12 demonstrate that the high activity of $Pt/CoO_x/SiO_2$ in CO oxidation is related to the absence of CO inhibition effects at low temperatures. On the basis of these results it was proposed that CoO_x is the supplier of O, which reacts with CO adsorbed on Pt. It is likely that the reaction takes place at the $Pt-CoO_x$ interface.

An interesting observation is that CO_2 can form on Pt(111) at the low temperature of 160 K upon heating the surface which is covered with
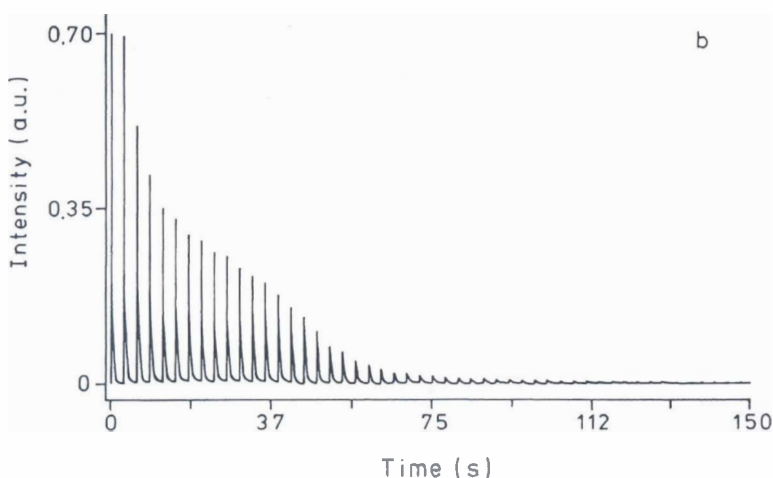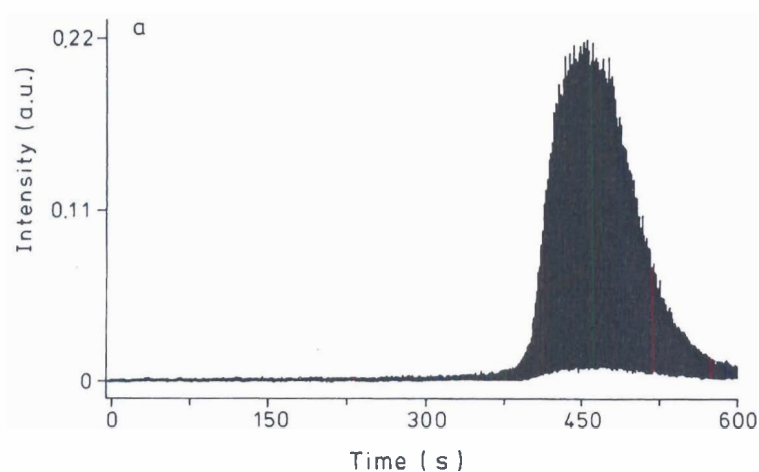
FIG. 12. Multipulse experiments with Pt/SiO_2 and $Pt/CoO_x/SiO_2$. CO_2 signal intensity: (a) CO-precovered Pt catalyst at 327 K during O_2 pulses; (b) a CO-precovered Pt–CoO_x catalyst at 313 K during O_2 pulses [reproduced with permission from Mergler et al. (54)].

molecularly adsorbed O_2 and CO (55). The authors showed that both O atoms in $O_{2,ads}$ react to give CO_2:

$$O_{2,ads} + 2CO_{ads} \rightarrow 2CO_2. \tag{11}$$
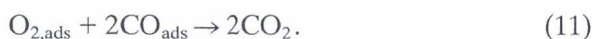
The CO_2 formation temperature coincides with the temperature at which $O_{2,ads}$ dissociates. Therefore, the origin of CO_2 formation at this low temper-

ature may be attributed to a reaction of the recently discovered "hot" O atoms with adsorbed CO. Recent articles have discussed chemical energy which is released during dissociation and subsequent formation of the strong metal–O bonds and is transformed in part into kinetic energy. This excess kinetic energy could cause motion of the adsorbed particles or could induce chemical reaction. STM is an obvious technique to use to characterize the distance that the adsorbed atoms can travel across the surface. This technique was applied by Wintterlin et al. (56) to investigate the diffusion distance of adsorbed O atoms when formed on Pt(111) by O_2 dissociation. The authors found evidence for the existence of hot O atoms. However, the O atoms created by dissociation appear in pairs, with an average distance of only two lattice atoms, which is much smaller than that found by the same group (57) for dissociation of O_2 molecules on Al(111). (On Al(111), the distance exceeds 80 Å).

The existence of hot O adatoms was also believed to be responsible for the desorption of CO_2 at 140 K from the Pt(100) hex surface partly covered with CO_{ads} and $O_{2,ads}$. Fadeev et al. (58) used TPR and high-resolution EELS (HREELS) to investigate CO oxidation on Pt(100). Some of the results are summarized in Fig. 13.

At 90 K, O_2 is adsorbed both on the reconstructed Pt(100) (hex phase) and on the nonreconstructed Pt(100) (1×1) surface as peroxide O_2, with the O–O bond axis parallel to the surface. This molecularly adsorbed
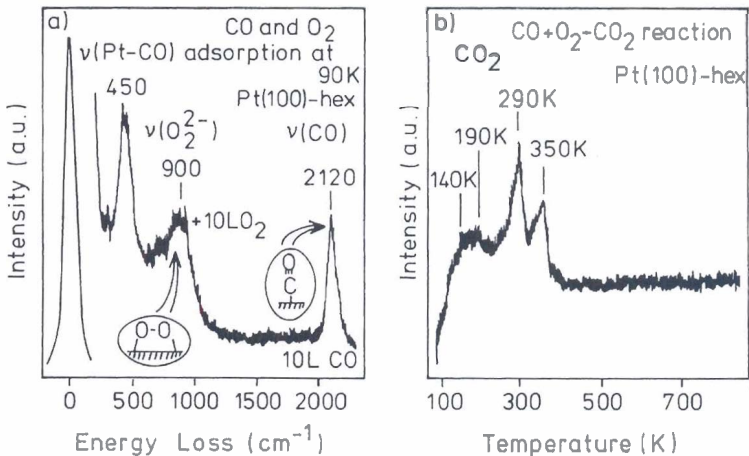

FIG. 13. Low-temperature CO and O_2 adsorption (a) and CO_2 desorption as a result of $CO_{ads} + O_{2,ads}$ reaction (b) on Pt(100)-hex surface [adopted with permission from Fadeev et al. (58)].

state desorbs at temperatures near 140 K from the hex phase, without dissociation. However, on the (1×1) surface, partial dissociation occurs simultaneously with dissociation at 160 K. Interaction of O_{ads} with CO_{ads} results in the formation of two CO_2 peaks, at 290 and 350 K. In addition to these CO_2 formation peaks, two low-temperature CO_2 peaks were observed at 140 and 190 K.

It has been reported that the CO_2 molecules produced on Pt surfaces can eject into the gas phase with a translational, vibrational, and rotational energy in excess of that expected from the surface temperature (59, 60). The group of King (61) applied the technique of single-crystal adsorption microcalorimetry to the investigation of CO oxidation on Pt(110). It was found that when CO is dosed onto a saturated O overlayer, the product CO_2 molecules have an additional 9 ± 17 kJ mol^{-1} energy in excess of that expected for thermally accommodated molecules. However, when O_2 is dosed onto a CO overlayer, the product CO_2 molecules have an excess energy of 52 ± 21 kJ mol^{-1}. It was suggested that these highly excited CO_2 molecules are formed by reaction of CO_{ads} with hot O adatoms produced by the O_2 dissociation process.

Many of the results discussed in this paper were obtained on idealized models of real catalysts, usually single-crystal surfaces investigated at low pressure. The obvious advantage of this approach is that these surfaces can be characterized on the molecular/atomic level by use of surface science techniques. Can we extrapolate these results to the behavior of supported catalysts with high surface areas at elevated pressures? In this context, the two main questions are (i) What is the effect of the pressure gap? and (ii) What is the effect of the structure gap? In many studies, both questions have been addressed because of their general importance to the understanding of catalysis with the aid of idealized models based on the ultrahigh vacuum surface science approach. Fortunately, sufficient information is available for the CO oxidation on both real and model catalysts to discuss these topics in detail for this reaction. In modern surface science equipment, the kinetics of the reaction can be followed in a microcatalytic reactor coupled to (but isolated by a valve from) the ultrahigh vacuum chamber. The pressure gap in the kinetics is then eliminated, and the structure effect can be examined. The chemical and physical state of the model catalyst is analyzed in the ultrahigh vacuum chamber by transfer under vacuum from the reactor to the analysis chamber.

The CO oxidation is usually considered to be a typical example of a structure-insensitive catalytic reaction. For example, the catalytic activity is almost equal on Pt/Al_2O_3 catalysts with widely varying particle sizes at high CO concentrations (7). However, the reaction becomes structure sensitive in excess oxygen. The observed temperature dependences of the

steady-state rates are almost similar on Pd(111), (100), (110), and (210) and polycrystalline Pd surfaces (38). Boudart (62) concluded that under similar experimental conditions the rate per Pd atom is equal on small Pd clusters ($\sim$5 nm) and Pd(111). Hence, data observed with a number of both single-crystal and supported metal catalysts indicate that the reaction is essentially surface insensitive.

However, Goodman et al. (63, 64) concluded that the CO oxidation on Pd is affected by the surface structure in a subtle manner. These authors combined kinetic and reflection absorption infrared spectroscopy (RAIRS) studies of CO oxidation on Pd(111) and (100) surfaces in the pressure range up to 10 mbar. RAIRS was used to follow the CO coverage during reaction. In the low-temperature range studied with first-order oxygen and negative first-order CO partial pressure dependencies of the rate, the apparent activation energy equals the heat of CO adsorption. The variation in heat of CO adsorption with coverage differs for Pd(111), (110), and (100). For example, at $\theta_{CO} = 0.50$, the heats of adsorption are 71, 139, and 122 kJ/mol for the (111), (110), and (100) surfaces, respectively. The authors argued that the reported apparent structure insensitivity of the reaction on Pd catalysts may be due to the varying CO coverages of the different surfaces under similar reaction conditions. Clearly, Fig. 9 illustrates that the reaction may be very sensitive to the surface structure under certain experimental conditions. A reactive mixture of CO and O_2 could also modify the catalyst particle shape in such a way that one type of surface structure dominates, leading to structure insensitivity. Another explanation could be that only the activity of one type of site is measured under certain experimental conditions. Results of Ramsier and Yates (5) are consistent with this model. They found from temperature programmed reaction experiments that the CO + O_2 reaction takes place at lower temperatures on the terraces than on the steps of the Pt(211) surface. However, at higher temperatures the high diffusion rate of O adatoms over the surface obscured the differences of step and terrace sites.

Detailed information is also available for the CO oxidation reaction on Rh. Peden (65), Peden et al. (66), and Oh et al. (67) compared the turnover rates of CO oxidation on Rh(111) and Rh(100) surfaces with those obtained on supported Rh catalysts with high surface areas. Figure 14 is a summary of some of the main results obtained for a CO and O_2 pressure of about 10^{-2} bar. Obviously, there is no intrinsic sensitivity of the reaction to the surface structure under these experimental conditions. Furthermore, Fig. 14 demonstrates that the single-crystal surfaces are in fact very good models for the practical catalysts.

Su et al. (68) investigated the reaction and the nature of CO adsorbed on Pt(111) at pressures up to 1 bar, characterizing the surface with sum
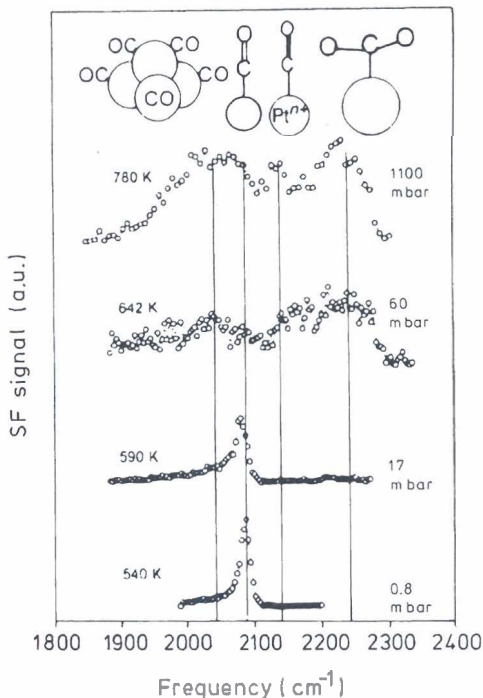
FIG. 15. *In situ* sum frequency generation spectra of CO oxidation on Pt(111) at different temperatures. The corresponding turnover rate (TOR) is also shown. The initial reaction conditions were 130 mbar O_2–50 mbar CO [adopted with permission from Su *et al.* (*68*)].

cm^{-1} peak. It was suggested that the metal carbonyl clusters are the reaction intermediates. The activation energy of the reaction decreases from 176 kJ/mol^{-1} at temperatures below 600 K (with a negative order of reaction in P_{CO}) to 59 $kJ \ mol^{-1}$ at higher temperatures (with a positive reaction order in P_{co}). Su *et al.* (*68*) concluded that the reaction mechanism changed at 600 K. I believe that the observed change in apparent activation energy is in fact consistent with those reported earlier for low-pressure measurements. The E_{act} for the reaction (59 $kJ \ mol^{-1}$) is within experimental accuracy equal to that found by Campbell *et al.* (*40*) for the CO + O_2 reaction on Pt(111) at low pressure, starting with an O-covered surface. STM studies show significant reconstruction of Pt(110) in both CO and O_2, whereas the surface structure of Pt(111) exhibits only minor changes (*68*).

As discussed previously, at relatively low temperatures the surfaces of Pt, Rh, and Pd are predominantly covered by adsorbed CO. At higher temperatures and/or under strongly oxidizing conditions, the metal surface

can become oxidized. CO oxidation rates on the surfaces of oxidized Pd and Rh are much lower than those on reduced surfaces. This effect is large for Rh (65). However, Pt showed no significant deactivation even under severely oxidizing conditions. Bowker *et al.* (69) reported that the reaction is sensitive to the surface structure at high temperatures when Rh surfaces are covered by O. Recent STM results demonstrated the high mobility of surface metal atoms as manifested in adsorbate-induced surface reconstructions, in particular by oxygen. CO can also induce changes in surface structure and even in morphology of the metal particles. This effect was demonstrated with the field ion microscope. An original hemispherial Rh tip becomes faceted by reaction with 10^{-4} Pa CO at 420 K. The resulting tip shape is that of a polyhedron with large (100) and (111) facets (70).

IV.   Reduction of NO by CO and H_2

In Section II.A, it was shown that the decomposition of NO proceeds on Pt, Pd, and Rh surfaces. However, it is not an efficient process and probably contributes only slightly to the NO removal. Exhaust gas contains the reducing gases CO, H_2, and various hydrocarbons, with H_2 produced by the water gas shift reaction

$$CO + H_2O \leftrightarrows H_2 + CO_2 \tag{12}$$

and by cracking of hydrocarbons. It is assumed in many papers that CO is mainly responsible for the NO conversion (71). The role of hc in conversion of NO has largely been neglected. Recent work by van den Brink and McDonald (72) suggests that CO mainly contributes to the conversion of O_2, whereas hcs have a significant role in NO conversion. Hydrogen, the concentration of which is about one-third that of CO in the exhaust, is a more efficient reducing gas for NO than CO at low temperatures (73).

Unfortunately, due to the presence of various gases in the exhaust, dinitrogen is just one of a variety of reaction products that can be formed in the catalytic converters used in automobiles. The main undesirable reaction products are N_2O and NH_3, which are formed especially under reducing conditions. Some of the processes that have been proposed involve adsorbed isocyanate (NCO) and adsorbed HNCO as intermediates. The formation of NCO_{ads} complexes has been observed on supported metals by IR spectroscopy. It has been established that the presence and the stability of the NCO groups depend on the support (74). It is most likely that the isocyanate species resides mainly on the support and its role is merely that of a spectator.

The reduction of NO_x by hc on noble metal surfaces has not been investi-

gated in detail using the surface science approach. The recent finding that NO reduction by hc significantly contributes to NO conversion is likely to stimulate fundamental investigations of NO–hc interactions on metal surfaces. IR studies by Bamwenda *et al.* (75) point to the presence of NCO and CN species on Rh/Al_2O_3 during the NO–propene reaction. Van Hardeveld *et al.* (76) investigated the reaction of C_2H_4 and NO on Rh(111) by temperature-programmed reaction spectroscopy (TPR) and SIMS. No indication was found of a direct reaction between the molecular species. The first steps are NO dissociation and ethylene decomposition. The dominant reaction products are, as expected, H_2O, CO_2, and N_2. At low NO–C_2H_4 ratios (<3), significant amounts of H_2, CO, and HCN are produced. Surface cyanide is formed by reaction of C_{ads} with N_{ads} in the absence of O_{ads}. Depending on the availability of hydrogen, CN_{ads} can be hydrogenated to give HCN that desorbs at the reaction temperature. (In earlier papers on automotive catalysis, the possible formation of HCN was proposed, but it has not been detected in the exhaust gas.)

Kobylinski and Taylor (73) studied the NO + CO and NO + H_2 reactions on supported noble metals and found that the activity for the first reaction increases in the order Pt < Pd < Rh < Ru and that for the second reaction Ru < Rh < Pt < Pd. The first reaction is slower than the second; only for Ru was the order reversed. Ru is an excellent catalyst for the NO reduction with a minimum of NH_3 production. However, Ru forms volatile oxides under operating conditions resulting in an unacceptable catalyst loss. The most efficient catalyst appears to be Rh (1).

Many techniques have been applied to examine the reaction pathways of the NO–CO and NO–H_2 reactions and to elucidate the reaction mechanisms. In this section some of the relevant results are discussed with emphasis on the reaction mechanism. Both the NO–CO and NO–H_2 reactions are discussed here since it is likely that the mechanisms of N_2 and N_2O formation are independent of the type of reducing agent. Note that CO dissociation is not considered to be involved in the mechanism. However, dissociative adsorption of NO into N and O adatoms is an important process on the relevant metals, as discussed in Section II.A. Possible mechanisms of N_2, N_2O, and NH_3 formation can then be evaluated on the basis of the following hypothetical mechanisms involving all the possible elementary steps in which NO_{ads}, N_{ads}, O_{ads}, CO_{ads}, and H_{ads} can participate:

N_2 formation

I. Without direct NO dissociation on the surface, the reduction may proceed via a bimolecular reaction between two molecularly adsorbed NO molecules:
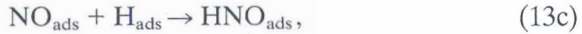
$$2NO \rightarrow N_2' + 2O_{ads}$$

or via a bimolecular reaction of NO_{ads} with CO_{ads}:

$$2NO_{ads} + 2CO_{ads} \rightarrow N_2 + 2CO_2. \tag{13b}$$

For hydrogen as reducing gas, a similar mechanism has been proposed via

$$NO_{ads} + H_{ads} \rightarrow HNO_{ads}, \tag{13c}$$

followed by $HNO_{ads} + H_{ads} \rightarrow N_{ads} + H_2O$ and combination of $2N_{ads}$ to N_2.

II. Dissociation of NO_{ads} followed by combination of 2N adatoms:

$$2N_{ads} \rightarrow N_2'. \tag{14}$$

III. Dissociation of NO_{ads} followed by reaction of N_{ads} with NO_{ads}:

$$N_{ads} + NO_{ads} \rightarrow N_2' + O_{ads}, \tag{15}$$

with N_2O_{ads} as an intermediate.

The oxygen adatoms formed by I–III may then react with H_{ads} or CO_{ads} as they do in the $H_2 + O_2$ and $CO + O_2$ reactions, although the presence of N_{ads} and NO_{ads} may modify the activation energies for these reactions due to lateral interactions. The N_2, CO_2, and H_2O desorb as soon as they are formed.

IV. A fourth proposed mechanism proceeds as follows:

$$2NO_{ads} + 2O_{ads} \rightarrow 2NO_{2,ads} \leftrightarrows N_2O_{4,ads} \tag{16}$$

$$N_2O_{4,ads} \rightarrow N_2' + 4O_{ads}. \tag{17}$$

NH$_3$ formation

V. Hydrogenation of molecularly adsorbed NO with HNO_{ads} as an intermediate:

$$NO_{ads} + 3H_{ads} \rightarrow NH_3 + O_{ads}. \tag{18}$$
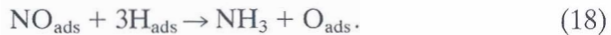
VI. Hydrogenation of N_{ads} formed by NO_{ads} dissociation:

$$N_{ads} + H_{ads} \rightarrow NH_{ads} \tag{19}$$

$$NH_{ads} + H_{ads} \rightarrow NH_{2,ads} \tag{20}$$

$$NH_2 + H_{ads} \rightarrow NH_{3,ads} \tag{21}$$

$$NH_{3,ads} \rightarrow NH_{3,gas}'. \tag{22}$$

N_2O formation

VII. Reaction of N_{ads} with NO_{ads}:

$$NO_{ads} + N_{ads} \rightarrow N_2O'. \tag{23}$$

VIII. Via reaction between two molecularly adsorbed NO molecules:

$$2NO_{ads} \rightarrow N_2O' + O_{ads}. \tag{24}$$
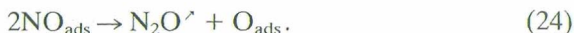
IX. Via dissociation of NO_{ads} and reactions between two N_{ads} and O_{ads}:

$$2N_{ads} + O_{ads} \rightarrow N_2O'. \tag{25}$$

The steps listed previously are the possible steps at very low NO conversions. At higher NO conversions, reactions of N_2, NH_3, N_2O, and H_2O with each other and the reactants should also be considered. In particular, decomposition of NH_3 and N_2O and reduction of N_2O may contribute to N_2 formation.

X.

$$N_2O \rightarrow N_2O_{ads} \rightarrow N_2' + O_{ads}. \tag{26}$$

XI.

$$NH_3 \rightarrow NH_{3,ads} \tag{27}$$

$$2NH_{3,ads} \rightarrow N_2 + 6H_{ads}, \tag{28}$$

via $NH_{2,ads}$, NH_{ads}, N_{ads}, and recombination of $2N_{ads}$. In addition to the previous steps, O_2 and NO formation via

XII.

$$2O_{ads} \rightarrow O_2 \tag{29}$$

and

XIII.

$$N_{ads} + O_{ads} \rightarrow NO_{ads} \tag{30}$$

have been documented in the literature.

In the presence of both H_2 and CO as reducing agents the situation will be even more complicated due to competition between CO and H_2 and, possibly, formation of specific products and intermediates such as HCN. This topic was addressed briefly at the beginning of this section.

Ample evidence exists for the major role of process II in N_2 formation on the noble metal surfaces, with the possible exception of Pt(111), as discussed later. Figure 5 shows that TDS of NO from a Rh filament following

a saturation exposure to NO exhibits two distinct N_2 peaks: β-N_2, with a maximum at about 625 K, and α-N_2, with a maximum at about 500 K. Similar behavior has been reported for Rh single-crystal surfaces, although the TDS of nitrogen from Rh(100)-like surfaces differ, significantly from those of the Rh(111)-like surfaces (28), as has been illustrated by the data of Fig. 6. At low NO exposures, no NO desorbs, and N_2 is evolved only in the β peak, which exhibits second-order desorption. Following higher NO exposures, α-N_2 desorption is observed at those NO coverages at which NO desorption is also observed, with a peak maximum only slightly lower than the α-N_2 peak. On the basis of these results, many authors assigned the β peak to N–N recombination (process II) and the α peak to process III. N_2O formation has been found for some supported Rh catalysts at the temperature regime of the α-N_2 and NO desorption peaks (77). This correlation between α-N_2, N_2O, and NO desorption may point to a common N_2O-like surface intermediate for α-N_2 and N_2O.

Lambert and Comrie (33) investigated the CO + NO reaction on Pt(111) and (110) surfaces and concluded that the reaction proceeds by a L–H mechanism between O_{ads} and molecular CO_{ads}. NO dissociation is also the prime step in the NO + H_2 reaction on a Pt foil at a pressure of 10^{-7} mbar (7). NH_3 was found to be the major product at temperatures lower than 600 K and N_2 was the major product at temperatures higher than 600 K when the NO/H_2 ratio was ~1/5.

Siera et al. (45) investigated the CO + NO reaction on the same surfaces and under the same experimental conditions as described for the CO + O_2 reaction. At low temperatures (<500 K), the reaction rate decreases in the order Pt–Rh(111) > (100) > (410) > (210). This is the same order as was observed for the CO + O_2 reaction, and it corresponds to the order in enthalpy of adsorption of CO, which increases from the (111) to the (210) surface. NO dissociation decreases in the order (410) ~ (210) > (100) > (111). For both reactions, the rate at low temperatures is controlled by CO desorption and not by NO dissociation activity.

Similar effects were found for the NO reduction by hydrogen on Rh single-crystal surfaces; Wolf et al. (21) studied the NO + H_2 reaction on several Rh surfaces by means of a scanning field emission probe-hole microscope. The temperature at which the reaction starts is strongly dependent on the NO coverage and is sensitive to the surface structure. At low NO precoverages and with hydrogen in the gas phase, the reaction starts already at 240 K on Rh(331), a surface with (111) terraces and (111)-like steps. On Rh(211), a surface with (111) terraces and (100) steps, the reaction starts at a significantly higher temperature. On Rh(321), a surface with (111) terraces and both (100)- and (111)-type steps, the reaction features characteristic of both (111) and (100) steps are observed. During reaction, an

electropositive adsorbate, assigned as $NH_{x,ads}$, is formed that dissociates at a temperature of approximately 300 K. At high NO precoverages, NO desorption is the initiation process; vacancies required for NO dissociation and hydrogen adsorption are then created. Under these conditions, surface structural effects are related to differences in enthalpy of adsorption of NO. However, hydrogen has a beneficial effect on the initiation temperature; increases of hydrogen pressure result in decreases of the onset temperature of the reaction. This effect can be explained in terms of hydrogen-assisted NO desorption, i.e., displacement of NO_{ads} by hydrogen. It is not a direct hydrogen-assisted NO dissociation, for example, by formation of HNO_{ads}. At low NO precoverages, the influence of the surface structure is related to the intrinsic differences in NO dissociation reactivity of the various surfaces. The observed onset temperatures of reaction did not differ significantly from the NO dissociation temperatures. The authors concluded that hydrogen-assisted NO dissociation proposed by Chin and Bell (77) does not seem to be important under their conditions (21).

Recently, spectroscopic techniques and the use of isotopically labeled N have provided a wealth of novel information about the mechanisms of N_2, NH_3, and N_2O formation. It is illustrative to discuss the detailed studies reported by Hirano et al. (78–80) concerning the mechanisms of the $NO + H_2$ reactions in light of recent studies. The surface investigated in most detail by Hirano et al. was a Pt–Rh(100) alloy surface (75% Rh and 25% Pt in the bulk).

The (1×1) structure, representative of the clean Pt–Rh(100) surface, changes into the $c(2 \times 2)$ surface structure after exposure to a reaction mixture of 1×10^{-7} mbar NO and 5×10^{-8} mbar H_2. Analysis of the $c(2 \times 2)$ surface by means of TDS, auger electron spectroscopy (AES), and HREELS indicated that atomic nitrogen was the main species present. For comparison, similar experiments were carried out on the Rh(100), Pd(100), and Pt(100) surfaces (78–80). Figure 16 illustrates some of the results.

Accumulated N atoms ordered in the $c(2 \times 2)$ surface structure were found on both Pt–Rh(100) and Rh(100) but not on Pt(100). In the presence of H_2 or D_2 at a crystal temperature of 400 K, a nitrogen–hydrogen vibration was found. Its intensity depends strongly on the partial pressure of hydrogen. Evacuation of H_2 and D_2 results in a quick loss of the signal. On the basis of these results, it was concluded that hydrogenation of N can occur via the reaction

$$N_{ads} + xH_{ads} \leftrightarrows NH_{x,ads}. \tag{31}$$
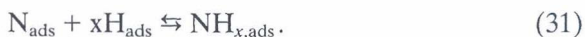
The hydrogenation of atomic nitrogen is largely reversible. By AES it was established that the N/Rh signal ratio was decreased only slightly
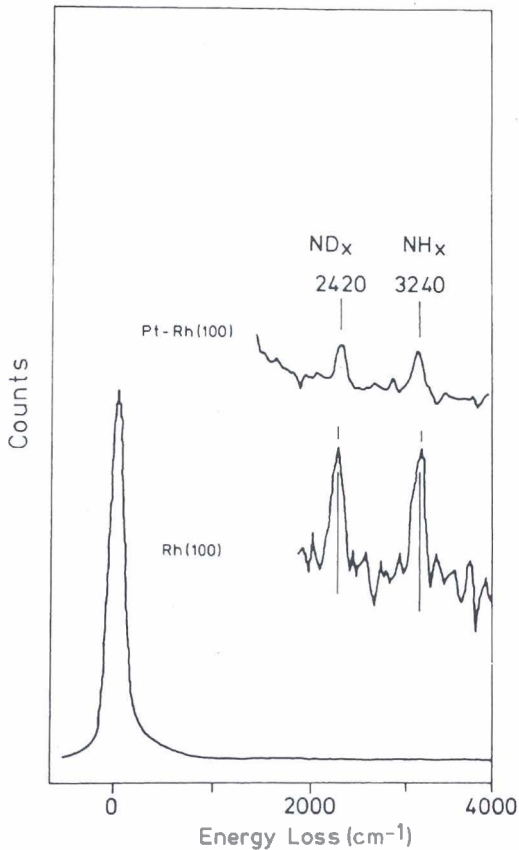
FIG. 16.   *In situ* EEL spectra of c(2 × 2)–N on the Rh(100) and Pt–Rh(100) surface in equilibrium with a hydrogen–deuterium mixture at 10^{-7} mbar and a temperature of 400 K. The intensity of the N–H signal is 1.6 times larger on Rh(100) than on Pt–Rh(100) [reproduced with permission from Nieuwenhuys *et al.* (*80*)].

during the hydrogen treatment. This result indicates that complete hydrogenation of the atomic nitrogen to NH_3 can occur but with a very low rate and only under these experimental conditions. The intensity of the N–H EELS signal varies with the square root of the hydrogen pressure:

$$I_{N-H} = A P_{H_2}^{1/2}. \tag{32}$$

Furthermore, N–H scissor vibrations were absent from the EELS spectra. On the basis of these observations it was concluded that the dominant NH_x adsorption complex is NH_{ads} and not $NH_{2,ads}$ or $NH_{3,ads}$.

Attempts to form a N layer on the Pt(100) surface by means of the $NO-H_2$ reaction were unsuccessful. The NO and H_2 partial pressures were varied from 10^{-8} to 10 mbar and the temperature from 400 to 600 K. Formation of a nitrogen overlayer was not observed under these conditions.

Useful information concerning the reactivity of adsorbed species is obtained by TPR. In the presence of a NO + hydrogen (H_2 or D_2) flow ($\sim 2 \times 10^{-7}$ mbar), the greatest ammonia formation was observed at approximately 500 K (heating rate, ~ 3 K s^{-1}) (78–80). However, if the surface was covered with ^{15}N prior to exposure to the ^{14}NO + hydrogen flow, ammonia resulting from ^{15}N was found even at 435 K (78). These results show that N atoms on the surface can react with hydrogen to give ammonia at 435 K. On the basis of these observations and the HREELS results, it was concluded that hydrogenation of atomic nitrogen via NH_{ads} is most likely the reaction route to ammonia formation (process VI).

Evidence for the presence of $NH_{x,ads}$ species has been obtained for many surfaces, including those of Pt–Rh (78, 80, 81), Pt (82–84), Rh (70–81, 85), Pd (81), and Ru (86). Sun et al. (84) investigated the stability of NH_x species on Pt(111) formed by electron-induced dissociation of $NH_{3,ads}$ using HREELS and XPS. $NH_{2,ads}$ formed following electron irradiation at 100 K. Upon heating, many of the $NH_{2,ads}$ species are rehydrogenated and desorb as NH_3 at temperatures of about 200 K, whereas a small fraction dehydrogenates, forming NH_{ads} at temperatures near 300 K. At temperatures exceeding 400 K, NH_{ads} dehydrogenates, leaving N_{ads} on the surface, which then desorbs as N_2 at temperatures between 500 and 700 K.

Recent SIMS spectra of the Rh(111) surfaces obtained during hydrogenation of atomic N_{ads} indicate that N_{ads} and $NH_{2,ads}$ (not NH_{ads}) are the predominant surface intermediates on Rh(111) (85). According to the authors, the third hydrogenation step in process VI, i.e., the hydrogenation of $NH_{2,ads}$ to give $NH_{3,ads}$, is rate limiting for NH_3 formation, with an activation energy of 69 kJ/mol.

Because of the interest in ruthenium as a potential catalyst for ammonia synthesis from N_2 and H_2, the hydrogenation of N_{ads} on Ru surfaces has been investigated (86). Both NH_{ads} and $NH_{2,ads}$ were found, in addition to $NH_{3,ads}$. Dietrich et al. (86) reported that the thermal stability of NH_{ads} is the highest of the three $NH_{x,ads}$ species ($x = 1, 2,$ and 3) on Ru(0001) and on Ru(1121) at temperatures up to 400–450 K. On Ru (1010), however, the thermal stability of $NH_{2,ads}$ is higher than that of NH_{ads} and much higher than those on other Ru surfaces. The reason for the enhanced thermal stability of $NH_{2,ads}$ on Ru(1010) is not clear. It was also found that coadsorbed N has a positive effect on the thermal stability of NH_{ads} on Ru(0001), whereas NH_{ads} is stable at temperatures up to 400 K, and NH_{ads} in the N/NH coadsorbate is stable at temperatures up to 460 K.

Yamada and Tanaka (*81*) found that the N c(2 × 2) structure on the (100) surfaces of Pd, Rh, and Pt–Rh does not change significantly upon the formation of NH_{ads} in the presence of hydrogen. This observation was interpreted on the basis of formation of NH_{ads} at the borders of c(2 × 2) islands during exposure to hydrogen.

An interesting effect of the surface structure was also found for Pt by Zemlyanov *et al.* (*82, 83*). HREELS and TDS confirmed that NO desorbs completely from Pt(111) without dissociation. However, N_2 and NH_3 formation were found upon heating the NO-covered Pt(111) surface in a hydrogen atmosphere. HREELS results were interpreted in terms of formation of HNO_{ads}. It was proposed that NH_3 and N_2 are formed without direct dissociation of NO:

$$HNO_{ads} + H_{ads} \rightarrow N_{ads} + H_2O', \tag{33}$$

followed by reaction II and hydrogenation of N_{ads} to NH_3. On Pt(100), N_{ads} formed by NO dissociation at 300 K reacts readily with hydrogen to give $NH_{2,ads}$ on the Pt(100) (1 × 1) surface and to give NH_{ads} on the reconstructed Pt(100)-hex surface. It was proposed that the NH_{ads} and $NH_{2,ads}$ species are the intermediates for NH_3 formation. However, NH_3 formation was not observed under the experimental conditions; the only product observed was dinitrogen.

The presence of HNO_{ads} was also proposed by Williams *et al.* (*87*) [on the basis of surface-enhanced Raman spectra (SERS)] as an intermediate for the NO + H_2 reaction on polycrystalline Rh films. The authors demonstrated that SERS can be used to characterize adsorbed species for CO + NO and NO + H_2 reaction (*87, 88*) on ultrathin Rh films deposited on a roughened gold substrate. (The Rh surface contained carbonaceous contaminants and possibly gold atoms.) This type of measurement is interesting because it yields vibrational data *in situ,* even at high pressures. In the presence of a NO + N_2 flow (ratio NO/H_2 = 1, total pressure-1 bar), a band characteristic of N_{ads} is present, and at temperatures from 420 to about 620 K, a band attributed to HNO_{ads} is present. The feature observed was attributed to HNO_{ads} because the surface species was formed only from NO_{ads} and hydrogen and not from N_{ads} and hydrogen. The authors proposed an additional pathway for NO dissociation, illustrated by Eq. (33).

This proposed process may explain the hydrogen-assisted NO dissociation first proposed by Hecker and Bell (*89*). Investigations of Rh single-crystal surfaces have also indicated that the presence of hydrogen may have a beneficial effect on NO dissociation (*21, 90*). It was also proposed that this alternative process for NO dissociation may be fast under conditions of slow direct decomposition because of the absence of free adjacent sites needed for NO dissociation (*87*). It was argued that a high coverage of

H_{ads} may block the vacant sites and slow the direct dissociation. [Blocking of sites needed for NO dissociation by hydrogen is an unlikely process, in contrast to blocking by NO, CO, N, or O. Furthermore, the hydrogen-assisted NO dissociation can also be attributed to the removal of O_{ads} and/or N_{ads} by hydrogen (21).]

The NO + H_2 reaction catalyzed by Rh(533), which is composed of four-atom-wide (111) terraces separated by (100) steps, was investigated *in situ* by Cobden *et al.* (91) in the 10^{-6} mbar pressure range by using fast XPS and mass spectrometry. The emphasis of this study was on understanding the oscillatory behavior of the NO + H_2 reaction on Rh surfaces. Some of the results are also relevant to the current discussion. It was shown that NO_{ads} is not present on the surface in the temperature range in which N_2 and NH_3 formation is observed. Two different N_{ads} species were observed in addition to O_{ads}. One N_{ads} species (NI) is probably N_{ads} on the (111) terraces, and the other (NII) is either N_{ads} adsorbed on the steps or $NH_{x,ads}$. O_{ads} plays an important role in controlling the surface reactivity. O_{ads} present in small amounts destabilizes the NI species, and at high O_{ads} coverage it favors the formation of NII.

The results summarized previously show that the surface structure and the presence of coadsorbed species have a large effect on the relative stability of NH_{ads} and $NH_{2,ads}$. However, more detailed studies are required to understand the relative stabilities of NH and NH_2 on noble metal surfaces. In conclusion, there is ample evidence that process VI is a major mechanism for NH_3 formation. The intermediates NH_x have been identified. The only possible exception may be Pt(111).

As stated in Section II.A, NO dissociation is negligible on Pt(111) at low pressure. However, Pt(100) is active in NO bond breaking. Polycrystalline Pt surfaces have low activity for NO dissociation. The group of Schmidt (92, 93) investigated the NO + CO reaction on polycrystalline and single-crystal Pt surfaces. At low pressures, Pt(111) is unreactive for the reaction. The kinetics of the reaction was investigated on polycrystalline Pt at temperatures from 300 to 1200 K and pressures from 10^{-8} to 1 mbar. The authors proposed that the reaction is a true bimolecular reaction between NO_{ads} and CO_{ads} (Eq. 13b) rather than NO decomposition with CO scavenging of O_{ads} (mechanism II). For the reactive Pt(100) surface, the reaction of NO + H_2 was very similar to that of NO + CO, and mechanism II qualitatively explains the observations.

The possible relevance of mechanisms I and IV to the formation of N_2 in TWC has not been addressed, except for polycrystalline Pt. Mechanism IV has only been added for the sake of completeness since it has not been proposed for NO reduction catalyzed by TWC. This and related mechanisms have been proposed for the selective catalytic reduction of NO_x by hydrocar-

bons (94–96) and hydrogen (97) in the presence of O_2 and catalyzed by various zeolites containing metal ions in their cavities. The rate of N_2 formation is enhanced in the presence of excess O_2. In several proposed mechanisms, $NO_{y,ads}$ (with $y > 2$) plays a key role. These mechanisms, although probably not important for TWC, may play a role when dissociation of NO cannot occur due to the absence of adjacent metal atoms required for NO dissociation. Shelef and Graham (3) proposed that the high selectivity for N_2 production that distinguishes Rh from Pt and Pd catalysts may be rooted in the promotion of N pairing in $2NO_{ads}$ molecules before the N–O bond is broken. These authors noted that IR spectra of NO on well-dispersed Rh/Al_2O_3 catalysts point to the presence of dinitrosyl $(NO)_{2,ads}$, a species that is not found on Pt and Pd/Al_2O_3 catalysts. These adsorbed dinitrosyl species could represent a locus for the event of pairing of the nitrogen atoms. It is probable that $(NO)_{2,ads}$ is formed on ionic Rh sites. No experimental evidence supporting this mechanism is available for TWC.

The formation rates of N_2 and N_2O on Pt–Rh(100) as a function of crystal temperature are shown in Fig. 17a for a mixture of 1.2×10^{-7} mbar NO and 3.6×10^{-7} mbar H_2 under steady-state conditions (78–80). The N_2 and NH_3 formation rates increase rapidly as temperature rises from 400 K until the maximum rates are obtained at approximately 600 K for N_2 and at the significantly lower temperature of about 525 K for NH_3. Nitrous oxide (N_2O) is only a minor product under these conditions. N_2 production remains high and almost constant until a temperature of about 1000 K is reached, indicating that the reaction rate in this temperature range may be controlled by the collision frequency of NO on the surface. At higher temperatures, the formation rate drops. For reaction mixtures with excess hydrogen, the N_2 formation rate is almost independent of the hydrogen pressure (zero order) at temperatures from 600 to 800 K. The ammonia production is approximately first order in hydrogen over the whole temperature range of 400 to 800 K. N_2O formation is observed only at relatively high NO pressures, and it is only slightly affected by changing the hydrogen pressure. Under the conditions of these experiments ($P_{NO} < 5 \times 10^{-6}$ mbar), the N_2 formation remains at least a factor of 100 larger than the N_2O production rate.

In another series of experiments of H_2 in the gas flow was replaced by NH_3 and the ^{14}NO by ^{15}NO to allow examination of the distribution of the two types of N atoms over the N-containing products. Figure 17b shows the variation of dinitrogen formation rates with increasing temperature in the presence of a flow of 1.2×10^{-7} mbar of ^{15}NO and 3.0×10^{-7} mbar of $^{14}NH_3$. In the low-temperature range ($T < 800$ K), the rate of $^{14}N^{15}N$ formation is higher than the rate of $^{15}N^{15}N$ formation, which in turn is much
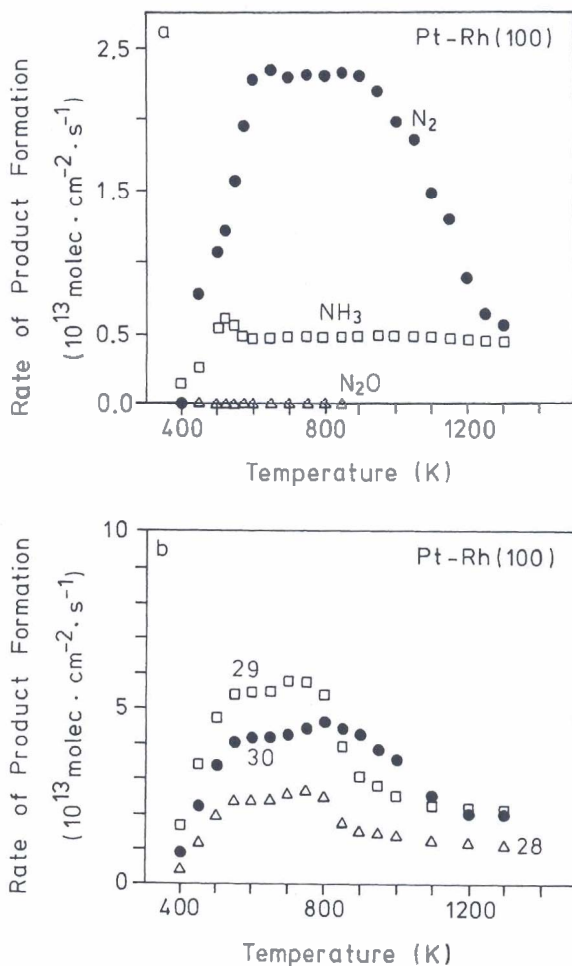
FIG. 17. (a) Steady-state formation of N_2 (●), NH_3 (□), and N_2 (△) on the Pt–Rh(100) surface in the presence of 1.2×10^{-7} mbar NO and 3.6×10^{-7} mbar H_2. (b) Steady-state formation rates of N_2 on Pt–Rh(100) with amu 28 (△), 29 (□), and 30 (●) in the presence of 1.2×10^{-7} mbar ^{15}NO and 3.0×10^{-7} mbar $^{14}NH_3$ [reproduced with permission from Hirano et al. (78)].

higher than the rate of $^{14}N^{14}N$ formation. [The ^{14}N ($^{14}NH_3$) concentration in the gas phase was a factor of 2.5 larger than the ^{15}N (^{15}NO) concentration.] The relatively low production of $^{14}N^{14}N$ is in qualitative agreement with results reported by Otto et al. (98) for the NO + NH_3 reaction catalyzed by supported Pt. Using N isotopes, these authors showed that N_2 formed

on Pt exclusively from NH_3 is only a minor path. Under the conditions used in the experiments shown in Fig. 17b, N_2 is formed on Pt–Rh(100) exclusively from NH_3, albeit at a much lower rate than from NO + NH_3 and from NO only. At temperatures higher than 700 K, the rate of $^{14}N^{15}N$ formation decreases rapidly with increasing temperature, and the $^{15}N^{15}N$ production increases. The $^{14}N^{14}N$ production shows the same temperature dependence as the $^{14}N^{15}N$ production.

The temperature dependence of the N_2 formation is the same for the NH_3 + ^{15}NO and the H_2 + NO reactions, suggesting that the same processes are involved. The N-combination reactions can occur over the whole temperature range, as demonstrated by the rate of $^{14}N_2$ formation. The production of $^{14}N_2$ is much smaller than the production of $^{14}N^{15}N$ and $^{15}N_2$, whereas the $^{14}NH_3$ concentration in the gas phase is a factor of 2.5 greater than that of ^{15}NO. This comparison may indicate that NH_3 is a slower producer of N_{ads} than is NO. However, this argument is in contradiction with the high rate of $^{14}N^{15}N$ formation. It was suggested that the relatively high rate of production of $^{14}N^{15}N$ may point to a large contribution of the reaction of N_{ads} with NO_{ads} (process III) to the N_2 formation in the lower temperature range ($T < 700$ K). At 1100 K, the rate of $^{14}N_2$ formation is a factor of 1.5 less than at 600 K; the rate of $^{14}N^{15}N$ formation is a factor of 2.5 less and the rate of $^{15}N_2$ formation only slightly lower. On the basis of this result, it was concluded that in the high-temperature range (1100 K), the importance of the N-combination reaction is much greater than in the low-temperature range and that ammonia becomes a less effective N producer than NO.

The same authors investigated the NO + H_2 reaction catalyzed by Pt–Rh(100) in the 10-mbar pressure range (78–80). Figure 18 shows some results obtained at 550 K.

At a temperature less than 500 K and a NO/H_2 ratio of 1/5, most of the NO reacts at low conversions to give N_2, and the formation of NH_3 is greater than that of N_2O. However, as the temperature increases above 500 K, the NH_3 production exceeds the N_2 production, and N_2O formation essentially ceases. The rate of NO conversion is much lower for a NO/H_2 ratio of unity than for the ratio of 1/5. N_2 production is only slightly affected by lowering of the H_2 pressure. However, NH_3 formation decreases drastically as a result of lowering of the hydrogen pressure. Consequently, the selectivity toward dinitrogen is much improved by lowering of the H_2/NO ratio. The hydrogen pressure was varied from 1.2 mbar to 24 mbar at a constant NO pressure of 1.2 mbar. It appeared that the reaction order in hydrogen is essentially zero for formation of N_2 and N_2O and about unity for formation of NH_3 under these conditions. It is emphasized that NO, NH_3, and N_2O decomposition and the NO + H_2 and NH_3 + NO
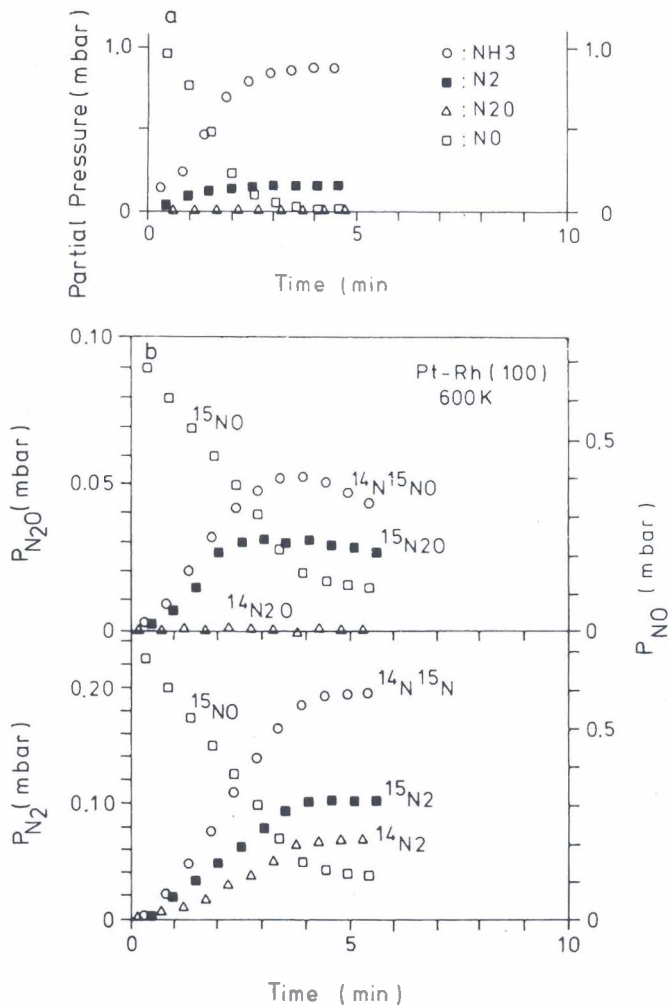
FIG. 18.   (a) Formation of N_2, NH_3, and N_2O on Pt–Rh(100) at 550 K at a NO/H_2 ratio of 1/5 with total pressure of 3 mbar. (b) The observed reaction products for the ^{15}NO + $^{14}NH_3$ reaction on Pt–Rh(100) as a function of the reaction time at 600 K with a $^{15}NO/^{14}NH_3$ ratio of 1 and total pressure of 3 mbar [reproduced with permission from Hirano et al. (78)].

reactions can occur simultaneously. Hence, useful information concerning one specific reaction is obtained only at the beginning of the reaction when the conversion is still low.

The most striking differences between the low- and higher pressure regimes are the following: (i) The relatively high selectivity to N_2O in the

higher pressure regime and (ii) the relatively high selectivity to ammonia. The first observation is completely in line with the expectations based on the mechanism for N_2O formation via process VII, requiring a high concentration of molecularly adsorbed NO. The dissociation of NO is inhibited by high concentrations of adsorbed NO, as discussed previously. It has also been reported that during the NO–hydrogen reaction a silica-supported Rh catalyst is largely covered with NO. On the other hand, in the low-pressure regime, Rh surfaces are covered with N_{ads}. As the temperature increases, the concentration of NO_{ads} decreases as a result of desorption and the selectivity to N_2O is expected to decrease, as observed.

The same argument can be used to interpret the relatively high selectivity to NH_3. A high concentration of N_{ads} favors a high selectivity to N_2 via process II. A low concentration of N_{ads} favors the formation of NH_3 (process VI). Obviously, the N_{ads} concentration at 600 K in the 10-mbar pressure regime is lower than that in the 10^{-7} mbar regime. It has been stated that the selectivity for NH_3 formation on supported metals such as Pt and Rh increases with increasing temperature up to a maximum T_m, beyond which it decreases; for Pd and Pt, T_m is about 600 K. The maximum temperature used in one investigation (78) was 600 K and, hence, the increasing selectivity to NH_3 observed when the temperature increases is in agreement with these data. The $^{15}NO + {}^{14}NH_3$ reaction was also investigated in the pressure range of 10 mbar (78). Some results are shown in Fig. 18b for a $^{15}NO/^{14}NH_3$ ratio of 1 at 600 K. $^{14}N_2O$ is not formed, whereas $^{14}N^{15}NO$ and $^{15}N_2O$ are both formed, showing that N_2O is formed only via process VII. At 600 K the formation of $^{14}N^{15}NO$ is faster than that of $^{15}N_2O$, which suggests that NH_3 is a better producer of N than NO at this temperature. $^{14}N_2$ formation is not detected at 550 K, whereas at 600 K the rate of $^{14}N_2$ formation is much less than that of $^{14}N^{15}N$ and $^{15}N_2$. On the basis of this observation it was suggested that process III is the dominant path for N_2 production in the low-temperature regime.

The molecular picture that the authors proposed from their results is the following (78–80): At low temperatures ($T < 450$ K), the majority of the adsorbed species are NO, and N is only a minor species. Adsorbed hydrogen is very mobile and can easily react with either O or N, provided it can find a vacant site in the neighborhood of an adsorbed O or N atom. The concentration of vacant sites is low in this temperature range. As the temperature increases, the concentration of NO becomes lower, and the concentration of N_{ads} increases. When the NO_{ads} concentration becomes much lower than the N_{ads} concentration, the rate of process VII, and hence the selectivity to N_2O, becomes low. For N_2 formation via process III, high concentrations of both N_{ads} and NO_{ads} are required; for N_2 formation via process II, a high concentration of N_{ads} is required. Consequently, process

III may contribute to the N_2 formation in the lower temperature range, and process II dominates in the higher temperature range. The selectivity to NH_3 increases with increasing temperature in the temperature range 300–600 K, again suggesting that the dominant mechanism of NH_3 formation is via process VI and not via hydrogenation of NO_{ads}. The selectivity of NH_3 will be the greatest at a temperature at which both the N_{ads} and H_{ads} concentrations are sufficiently high. The strong positive reaction order in hydrogen pressure shows that the concentration of H_{ads} is the limiting factor under the experimental conditions. At some very high temperature, the reaction rates of both NH_3 and N_2 formation become low because of the low N_{ads} and H_{ads} concentrations. Obviously, this temperature depends strongly on the absolute NO and H_2 pressures and on the metal surface. Rh, with its much stronger metal–N bond strength, will exhibit a much better selectivity toward N_2 than Pt, which has a weaker metal–N bond strength. The observed decrease in selectivity toward NH_3 as temperature becomes very high can be attributed to a combination of limited availability of H at high temperature and the high rate of NH_3 decomposition.

In contrast to the apparent structure insensitivity of the $CO–O_2$ reaction catalyzed by Rh and reported by Peden (65), Peden et al. (66), and Oh et al. (67), these researchers found substantially different kinetic behavior for the NO + CO reaction on Rh(111), Rh(100), and supported Rh/Al_2O_3 (66, 67), as illustrated in the Arrhenius plots of Fig. 19. The corresponding activation energies are 124 kJ/mol for Rh(111) and 101 kJ/mol for Rh(100). The authors postulated that the structure sensitivity of the CO + NO reaction catalyzed by Rh is due to different rates of NO dissociation. On Rh(111), the rate would be limited by the formation of N_2 from process II, and the surface would be largely covered with N_{ads}. On the supported catalyst, the rate-limiting step was judged to be NO dissociation.

STM is an attractive technique for elucidating reaction mechanisms since, in addition to the observation of the surface structure, it allows imaging of adsorbed atoms and molecules under some conditions. Many recent examples indeed show that STM can provide useful additional information (44, 99, 100). Leibsle et al. (100) observed a one-dimensional CO + O_2 reaction on Rh(110). Xu and Ng (99) imaged NO_{ads} molecules coadsorbed with O or N atoms on Rh(111); NO_{ads} molecules form ordered islands with (4×4) structure. Repulsive interactions between NO and O or N lead to segregation of NO and O or N islands. The results also suggest the formation of Rh–$N(1 \times 2)$ added row reconstruction through NO dissociation.

Some confusion exists in the literature concerning N_2O formation as a product of the CO + NO reaction. In the papers of Oh et al. (67) and Peden et al. (66), N_2O formation was not reported for the CO + NO reaction on Rh single-crystal surfaces. However, Hecker and Bell (101)
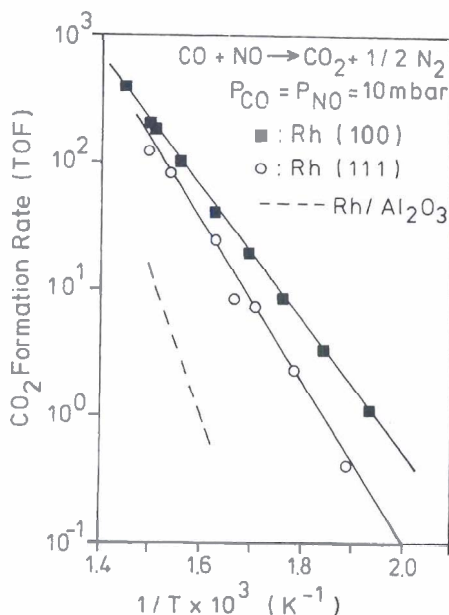
FIG. 19. Comparison of the specific rates of the NO–CO reaction on Rh(111), Rh(100), and Rh/Al$_2$O$_3$ at $P_{CO} = P_{NO} = 10^{-2}$ bar [adapted with permission from Oh et al. (67)].

reported that N$_2$O is a major N-containing product of the CO + NO reaction catalyzed by Rh/SiO$_2$. Belton and Schmieg (102) studied the reaction on a Rh(111) catalyst and found that N$_2$O is formed with a selectivity of 70% from a mixture of 1.06 kPa of NO and 1.06 kPa of CO at temperatures between 525 and 675 K. Both Rh(111) and Rh/SiO$_2$ give similar product distributions, with more N$_2$O than N$_2$ and an activation energy of 139 kJ at temperatures higher than 480 K.

To what extent does reaction III contribute to N$_2$ formation? Whereas Hirano et al. (78–80) concluded from that reaction III may make a significant contribution at low temperatures, Belton et al. (103) concluded that there is no experimental evidence for the reaction step

$$NO_{ads} + N_{ads} \rightarrow N_2O_{ads} \rightarrow N_2 + O_{ads}, \qquad (34)$$

and they recommended that in future NO reduction mechanisms this step should be omitted. Belton et al. prepared a Rh(111) surface covered with 0.4 monolayers of ^{15}N by electron beam dissociation of ^{15}NO$_{ads}$ and saturated this surface with ^{14}NO at 200 K. TDS did not reveal ^{15}NO, showing that scrambling of ^{15}N and ^{14}NO did not occur during their experiments. In addition, all three N$_2$ isotopic mixtures (masses 28, 29, and 30) have

been observed in the TDS, indicating that the α-N_2 feature is also due to N atom recombination. The apparent first-order behavior of the α-N_2 peak and the correlation of α-N_2 and NO desorption were attributed to rate-limiting formation of N_2 by the dissociation of NO_{ads} at high NO coverage (NO_{ads} inhibition of its own dissociation). Another view was presented by Borg *et al.* (*23*) and by Makeev and Slinko (*104*): Repulsive interactions in the adlayer are required to produce α-N_2. Bugyi and Solymosi (*105*) prepared a N overlayer with high coverage on Rh(111) from atomic N in the gas phase by means of a discharge tube and observed α-N_2 and β-N_2 desorption states very similar to those observed after NO exposure. Apparently, the presence of NO_{ads} is not required to produce α-N_2 in TDS. Makeev and Slinko (*104*) were able to simulate the TDS, reported by Root *et al.* (*106*) and Borg *et al.* (*23*), of N_2 and NO from Rh(111) following NO exposure on the basis of repulsive interaction between N_{ads} and NO_{ads}, together with the strong inhibition of NO dissociation by NO_{ads} N_{ads}, and O_{ads}.

The NO + CO reaction on Rh(111) was investigated by Permana *et al.* (*107*) by RAIRS. The measurements were performed with NO and CO pressures in the 10-mbar range and, hence, in the same range as in the automotive exhaust gas contacting the TWC. IR spectra taken under reaction conditions showed only atop CO and multiply bonded (either twofold or threefold) NO. Changes in the surface coverages of NO_{ads} and CO_{ads} correlated well with the observed changes in N_2O selectivity; at temperatures below 635 K, NO_{ads} dominates and N_2O formation is favored. At temperatures above 635 K, at which N_2 formation is preferred, CO is the majority surface species. Obviously, these RAIRS data support the model according to which N_2O and N_2 are formed by parallel pathways by reaction of N_{ads} with either NO_{ads} or N_{ads}, respectively. By adding $^{15}N_2O_{gas}$ to the ^{14}NO and ^{12}CO reactant mixture it was shown that $^{15}N_2O$ was not consumed during the reaction. Therefore, readsorption of N_2O is not an important path to produce N_2 under the conditions used in Permana *et al.* (*107*) (650 K and low conversion). However, the same authors also showed that N_2O is readily converted to N_2 at temperatures higher than 700 K (*102*). The CO + N_2O reaction runs only after complete NO conversion at temperatures higher than 700 K.

The mechanism and kinetics of the NO + CO reaction on Rh(111) have been discussed in detail by Zhdanov and Kasemo (*108*). They showed that simulations based on surface science data obtained at low pressures reproduce the scale of the reaction rate at the pressure regime of interest for the TWC but fail to predict accurately the apparent activation energy and reaction orders.

Can we conclude that process III does not at all contribute to N_2 forma-

tion? In this context it is relevant to review recent work of Ikai et al. (109–111) on N_2 desorption from Pd(110). They showed that the behavior of Pd(110) toward NO adsorption is very different from that of Pd(100). TDS experiments (with an NO-covered surface rapidly heated in uhv) characterizing NO adsorbed on Pd(110) showed NO, N_2, and N_2O peaks, with a maximum at about 490 K. In addition to the 490-K peak, a second NO desorption peak was observed at 370 K. The authors also measured the spatial distribution of the molecules desorbing during TDS and TPR. This technique can provide additional information about the nature of the chemical processes involved. N_{ads} can accumulate on Pd(100) during NO exposure at higher temperatures but not on Pd(110). N_{ads} accumulation on Pd(110) was obtained by exposing the surface to N^+/N_2^+ ions. The resulting N_2 TDS are distinctly different from the N_2 TDS observed following NO adsorption. In addition, its spatial distribution is very different from the off-normal desorption found for N_2 formed from NO adsorption and also from N_2 formed by the NO + H_2 reaction. In the same way, a Pd(110) surface precovered with ^{15}N was prepared. Exposure to ^{14}NO resulted in $^{15}N^{15}N$ peaks at 460 and 520 K. The spatial distribution is very different from that of $^{15}N_2$ at 460 K. Ikai (111) suggested that reaction III may be responsible for the off-normal desorption of N_2 at 490 K.

On the basis of the results discussed previously, it is concluded that the formation of N_2 on Rh(111) can be understood solely in terms of N_{ads} combination. However, it is premature to conclude that process III does not play any role in the N_2 formation on other metal surfaces.

The CO + NO reaction on various kinds of Pd catalysts was investigated by Rainer et al. (112). Kinetics data for Pd/Al$_2$O$_3$ and "planar model" Pd/Al$_2$O$_3$/Ta(110) catalysts were compared with those for CO + NO on Pd(111), (100), and (110) surfaces. Figure 20 is a comparison of the Arrhenius plots measured at partial pressures of about 1 mbar in each reactant for the model catalysts and at a CO pressure of 5.9 and a NO pressure of 6.8 mbar (in a helium carrier) for the Pd/Al$_2$O$_3$ powder catalyst.

The reported apparent activation energies are 67 kJ/mol for Pd(111) and (100), 71 kJ/mol for Pd(110), and 155 kJ/mol for the Pd/Al$_2$O$_3$ powder catalyst. The authors concluded from the comparison of rates per surface Pd atom (TOF) at 560 K that the supported Pd/Al$_2$O$_3$ powder catalysts exhibit a pronounced particle size effect, with an increase in activity with increasing particle size. The Pd(111) surface is more active than the (100) and (110) surfaces. The authors argued that the smaller Pd particles with their higher step/edge/defect densities have more in common with the open single-crystal faces, whereas the larger particles have more Pd(111) character. Pd(100) is more effective at dissociating NO$_{ads}$ than Pd(111). As a result, Pd(100) yields a higher ratio of N_2/N_2O than Pd(111). TDS of N_2
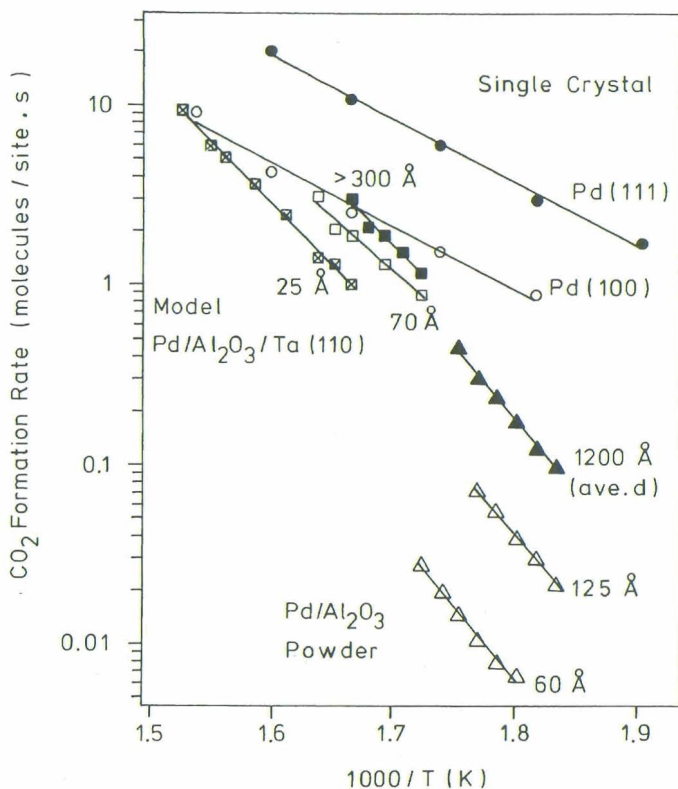
FIG. 20. Arrhenius plots for the rate of the NO–CO reaction on various kinds of Pd catalysts. The planar model and single-crystal surface data were taken in a batch reactor (1 mbar of each reactant) and the powder catalyst in a flow reactor ($P_{CO} = 5.9$ mbar, $P_{NO} = 6.8$ mbar) [adopted with permission from Rainer *et al.* (*112*)].

following NO exposure and TPR of CO + NO show essentially two peak maxima for N_2 production: α at 450 K and β between 530 and 590 K for Pd(111) and between 575 and 625 K for Pd(100). The desorption temperature for β-N is higher than the reaction temperature employed in these experiments. The Pd(100) surface, more active for NO dissociation than Pd(111), exhibits the lower activity for the reaction. This correlation implies that the removal of β-N is more important than NO dissociation in determining the reaction kinetics. Obviously, the dissociation of NO is not the rate-limiting step on Pd. The origin of the huge difference in activity between the model catalysts and the powder catalyst is not clear.

V.   Effects of Alloy Formation

In most of the early papers, the formation of alloy particles was considered to be undesirable. For example, Kummer (113) mentioned that each noble metal is used for a specific purpose which can be served by keeping it separate from other metal components. However, according to Nieuwenhuys *et al.* (114–116), alloy formation cannot be avoided at the extreme conditions under which the catalyst must operate. Many studies have shown that nearly all the noble metal particles are alloyed in real vehicle-aged catalysts (117, 118). Many possible detrimental effects of alloy formation have been proposed (113), including reduction of the effectiveness of Pt for alkane oxidation because of Rh surface segregation. In addition, Pt alloy formation may result in a loss of the availability of Rh or Pd to the exhaust gas since Pt readily sinters to large crystallites at temperatures higher than 870 K, whereas Rh and Pd alone can remain dispersed under usual operation conditions (113). Alloy formation in general may also result in a distinctly different behavior, relative to those of the pure component catalysts (119). Therefore, it is of particular interest to review the available data concerning the effects of alloy formation on the reactions of importance in automotive catalysis.

The first step in understanding the results of activity measurements with alloy catalysts is understanding knowledge concerning the surface composition. Under vacuum, Pd segregates to the surface of Pt–Pd (120) and Rh–Pd alloys (121). The surface composition of Pt–Rh alloys has been investigated by several groups with techniques such as AES, ion-scattering spectroscopy, work function measurements, atom-probe FIM, and STM (114–116, 119, 122–131). Most of the results point to a strong Pt surface segregation of clean Pt–Rh crystals under vacuum. The Pt enrichment in the top layer is accompanied by Pt depletion in the second layer (123, 124, 126). Calculations of LeGrand and Treglia (126) and Schoeb *et al.* (127) show that the experimentally found Pt surface enrichment can be understood on the basis of a difference in surface energy. Pt surface enrichment should be expected, whatever the bulk composition and equilibrium temperature.

According to van Delft *et al.* (114, 115), the surface composition of Pt–Rh alloys may be extremely sensitive to the presence of adsorbate atoms due to the very small differences in factors resulting in Pt surface segregation of the clean surfaces. Experiment show that the surface composition may easily change in the presence of other elements. Carbon monoxide and hydrogen do not exert a measurable influence on the surface composition (114, 115). For oxygen, however, a strong oxygen-induced Rh surface segregation was found that was caused by the much stronger Rh–O bond strength relative to that of Pt–O (114, 115, 124). Similar results were obtained for

NO adsorption. NO dissociates on the surface, resulting in oxygen-induced Rh surface segregation. The presence of sulfur also causes Rh surface segregation (123).

In view of the relative thermal stabilities of the oxides (Rh_2O_3 > PdO $\geqslant$ PtO_2), it is not surprising that under oxidizing conditions and at temperatures higher than 870 K, metallic Pt particles exist in combination with Rh oxide (132, 133) and that PdO crystallites separate from Pt crystallites in Pd–Pt alloys in the temperature range 670–870 K (134). A more complicated behavior was found for Pd–Rh (135).

Beck et al. (124) reported that the $Pt_{0.10}$–$Rh_{0.90}$ (111) single-crystal surface, which has a surface composition of about 30% Pt in vacuum, remains Pt rich, even under 50 mbar of hydrogen at temperatures typical of automotive catalytic converter operation 770–870 K. A few studies of supported Pt–Rh/ Al_2O_3 catalysts have been pursued using NMR spectroscopy. Wang et al. (136) used ^{13}C NMR of adsorbed CO as well as ^{195}Pt NMR and concluded that the surface is slightly enriched in Rh in the presence of CO. Savargaonkar et al. (137) reported the use of ^1H NMR spectroscopy to determine the surface composition of Pt–Rh/Al_2O_3 catalysts in the presence of hydrogen. The authors concluded that their catalysts are slightly enriched in rhodium relative to the adsorbate-free catalysts, which are enriched in Pt. Simulations indicated that the heat of adsorption of hydrogen must be 13 kJ/mol higher on Rh than on Pt to achieve the reported Rh surface segregation. It should be noted that the interpretation of the observed Knight shifts in terms of surface composition is not straightforward. Furthermore, literature data characterizing hydrogen adsorption on pure well-defined single-crystal surfaces suggest that the initial heat of adsorption of hydrogen on Rh (80 kJ/mol) is similar to that on Pt (within 10%) (138). In my opinion, there is no doubt of the correctness of the earlier conclusion: Pt–Rh surfaces are Pt enriched under reducing conditions and Rh enriched under oxidizing conditions.

The most direct determination of both the surface structure and the composition of Pt–Rh alloy surfaces was obtained with STM (128, 129). The (100) surfaces of $Pt_{0.25}$–$Rh_{0.75}$ and $Pt_{0.50}$–$Rh_{0.50}$ single crystals were imaged with atomic resolution and with discrimination of the Pt and Rh atoms. The STM image shown in Fig. 21 demonstrates that there is a limited tendency for Rh–Rh and Pt–Pt clustering on the surface, and Pt–Rh ordering is absent. Interestingly, Pt preferentially populates the step edges. Oxygen causes a large reconstruction of the surface (130, 131). For example, Fig. 22 shows the STM image of the (100) surface of $Pt_{0.25}$–$Rh_{0.75}$ exposed to O_2 at 770 K and subsequently cooled to room temperature in oxygen. The STM image points to the formation of linear Rh–O chains.

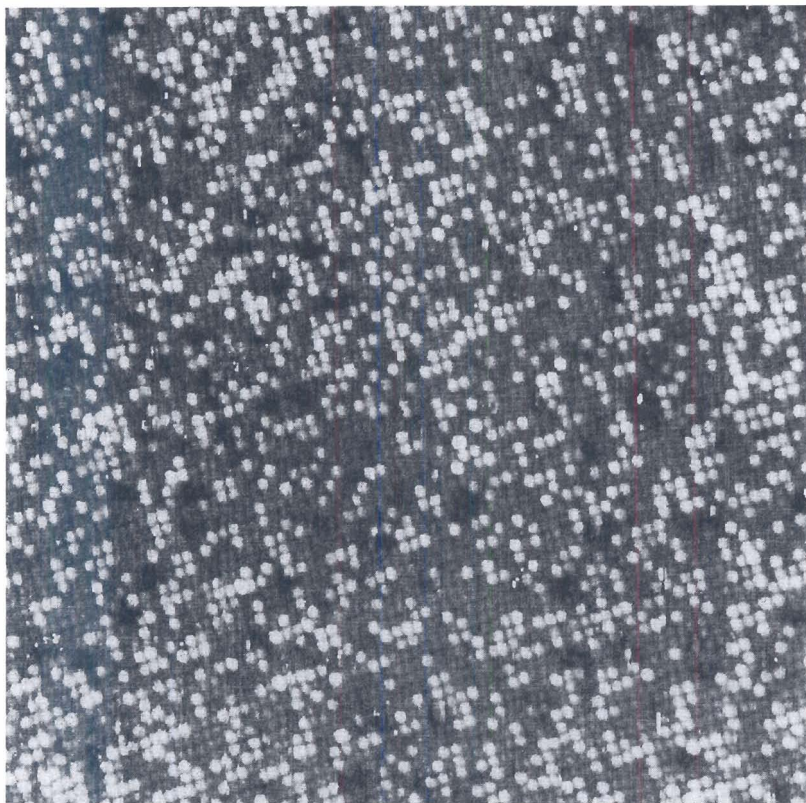Adsorption and reactivity investigations of Pt–Rh alloy surfaces were

FIG. 21. STM image of $Pt_{0.5}$–$Rh_{0.5}(100)$; image size, 200×200 Å. Bright spots correspond to Rh atoms [reproduced with permission from Wouda et al. (129)].

carried out in a number of laboratories, particularly to examine the effect of alloy formation on the reactions of importance in automotive catalysis: oxidation of CO, oxidation of hydrocarbons, and reduction of NO (45, 79, 80, 114–116, 139–147). NO bond breaking is usually considered the first step in the reduction of NO by CO and hydrogen and, therefore, many papers deal with studies of NO adsorption and dissociation (see Section II.A.4). NO adsorption is also a sensitive probe for examining the possible effect of alloy formation since there are large differences in the behavior of Pt and Rh toward NO interaction. The extent of dissociation of NO on Pt is sensitive to the surface structure. Rh has a much greater reactivity for NO bond breaking, and the effect of the surface structure is smaller.

At temperatures of about 210 K, complete dissociation of NO occurs on Rh(100) and on Pt–Rh(100) alloy surfaces at low NO coverages, and partial
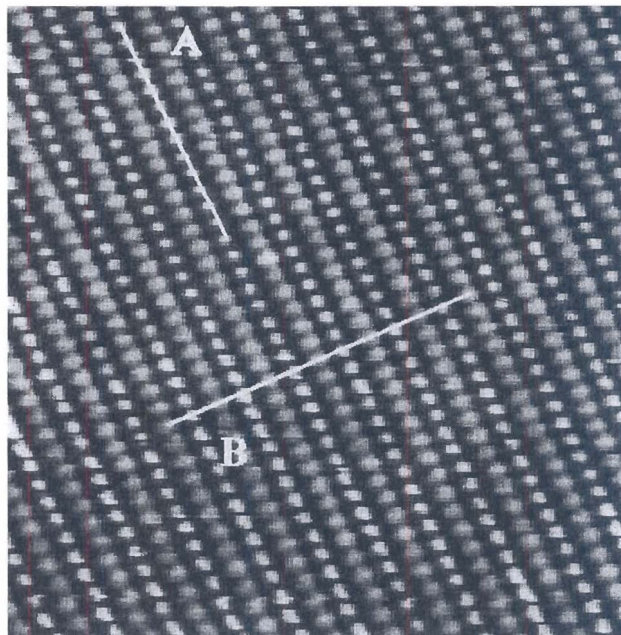
FIG. 22.   STM image of $Pt_{0.5}$–$Rh_{0.5}(100)$ exposed to O_2 at 770 K and subsequently cooled to room temperature in oxygen [reproduced with permission from Wouda *et al. (131)*].

dissociation occurs during heating following saturation. The extent of N_2 desorption is a measure of the activity of a surface in NO bond breaking. On the (100) surfaces of Pt, Rh, and $Pt_{0.25}$–$Rh_{0.75}$, NO desorption occurs at about 450 K. Figure 23 illustrates the effect of alloy formation on NO dissociation under TDS conditions. It shows the relative amount of NO desorbing as NO as a fraction of the total coverage following exposure at a temperature of 210 K or lower. On Rh(100) and on Pt–Rh(100) alloy surfaces, complete dissociation occurs at low NO coverages and partial dissociation occurs during heating following saturation *(141)*.

In contrast to the behavior on Rh(100) and Pt–Rh(100) surfaces, the fraction of NO decomposing on Pt(100) does not change dramatically with coverage. The behavior of the Pt–Rh(100) surface resembles that of the pure Rh(100) surface at low NO coverage and that of pure Pt(100) at high coverage. This pattern illustrates that Rh atoms on the surface are very effective in NO dissociation and that NO dissociation occurs mainly on Rh sites. These results also indicate that mixed Pt–Rh sites are not very reactive in NO bond breaking *(141)*.

NO dissociation is sensitive to the surface structure of Rh and, in particu-
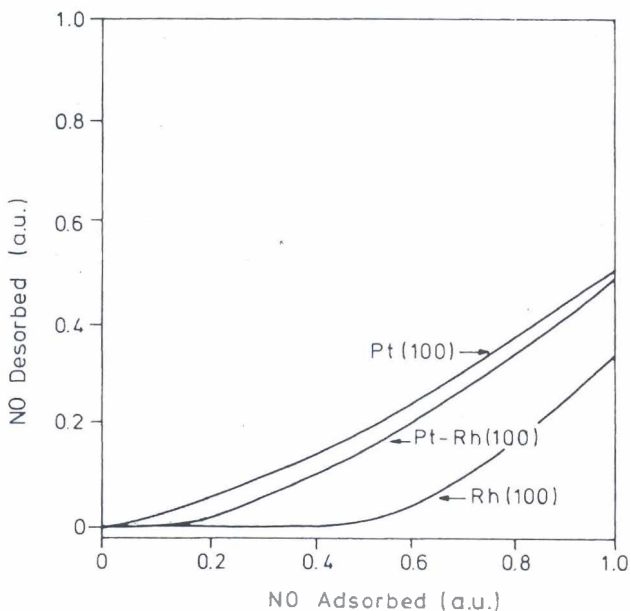
FIG. 23.   Molecular NO desorption from Pt–Rh, Pt, and Rh(100). The abscissa is NO adsorbed as a fraction of saturation NO coverage [reproduced with permission from Siera *et al.* (*141*); Pt and Rh(100) data from Root *et al.* (*106*) and Gorte and Schmidt (*148*)].

lar, to that of Pt. For example, it has been reported that the Pt(111) surface cannot break the NO bond, whereas the Pt(410) surface is very reactive in NO bond breaking (*27*). XPS has been used to investigate the NO dissociation on Pt–Rh single-crystal surfaces (*114*); the results are summarized in Fig. 24. This figure shows the following: (i) The dissociation activity is sensitive to the surface structure. The (410) and (210) surfaces are more reactive in NO bond breaking than the (321) surface, the activity of which is larger than that of the (111) surface. The effect of the surface structure is greater for Pt-rich than for Rh-rich surfaces; and (ii) the dissociation reactivity is higher for Rh-rich than for Pt-rich surfaces.

Fisher *et al.* (*143, 144*) investigated NO adsorption and reduction on the (111) surface of a $Pt_{0.10}$–$Rh_{0.90}$ single crystal with a surface composition of about 30% Pt in vacuum. The presence of 10 atom% Pt in the bulk significantly reduces the ability of the surface to dissociate NO. The activation energy of NO dissociation was reported to be intermediate between those of the reaction on Rh(111) and on Pt(111).

An interesting behavior was found for the Pt–Rh(100) surface after exposure to NO at 500 K (*139*). Initially, a c(2 × 2) surface structure is
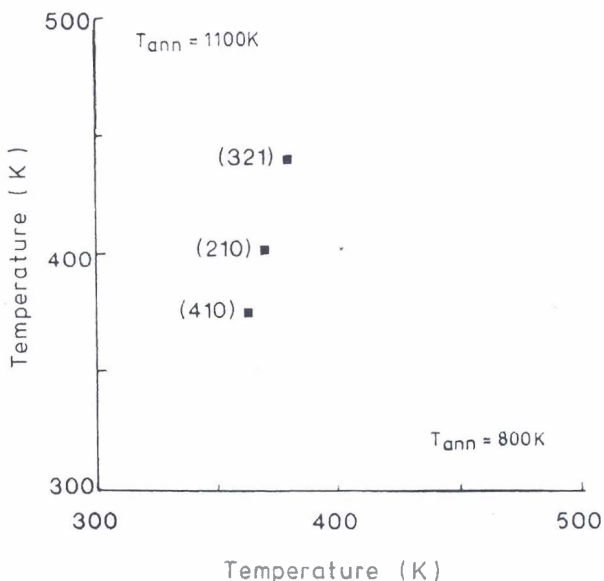
FIG. 24. The temperature at which a dissociation percentage of 25% is obtained for Pt-rich Pt–Rh alloy surfaces versus the same parameter for Rh-rich Pt–Rh alloy surfaces [reproduced with permission from Wolf *et al.* (*114*)].

formed which, via a combination of c(2 × 2) and (3 × 1), changes slowly into a (3 × 1) surface structure. The time required for formation of the (3 × 1) structure depends strongly on the initial Rh surface concentration. On Rh-rich surfaces, the (3 × 1) structure is formed much faster than on an originally Pt-rich surface. The O formed by NO dissociation slowly replaces the N adatoms also formed by NO dissociation. The O atoms extract Rh atoms to the surface. Since the second layer is Rh enriched, the slow formation of the (3 × 1) structure is related to an exchange of Rh and Pt atoms between the second and the top layer.

Similar observations were made by Tanaka *et al.* (*146, 147*) for Pt–Rh surfaces prepared by electrochemical deposition of Pt on Rh(100) or Rh on Pt(100). All these studies demonstrate that the first two layers of Pt–Rh samples are very flexible; both composition and structure change easily with changing experimental conditions caused by exchange of atoms between the first and second layer. A pure Rh(100) surface is not very reactive for NO reduction by hydrogen at temperatures <650 K. A Pt-enriched Pt–Rh(100) surface shows reactivity at temperatures higher than 650 K. However, on a Rh-enriched Pt–Rh(100) surface with (3 × 1) structure NO reacts with hydrogen even at 500 K. The authors suggested that a Pt–Rh(100) hybrid

surface with (3×1) structure is the active catalyst which can be formed during the catalytic process (*146, 147*).

In contrast to the activity of Pt(100), the activity of the Pt(110) surface is very low for the NO + H_2 reaction (*149*). Deposition of a submonolayer of Rh on this surface results in a drastic enhancement of the activity, which is also higher than that of pure Rh(110). The resulting $p(1 \times 2)$ Pt–Rh(110) catalyst exhibits an almost equally high activity as $p(3 \times 1)$ Pt–Rh(100). It was proposed that a specific Pt–RhO–Pt arrangement is needed for high activity (*149*).

The previous results show that Rh sites are those with the higher activity for NO dissociation. What do we know about CO adsorption? Does CO prefer Rh or Pt sites? These questions were addressed by Rutten *et al.* (*145*) in an investigation of CO adsorption on a $Pt_{0.25}$–$Rh_{0.75}$ (111) surface with RAIRS, TDS, and work function measurements. It was found that CO shows a pronounced preference for Rh sites at both 100 and 300 K up to a coverage of $\theta = 0.27$. Adsorption was found to be predominantly on atop sites, and only weak bridge bands were detected. Unfortunately, information concerning coadsorption of CO and NO on Pt–Rh single-crystal surfaces is missing. However, IR spectra of NO–CO mixtures are available for Pt–Rh supported on silica. Heezen *et al.* (*150*) concluded that for CO–NO mixtures the NO molecules are primarily adsorbed on Rh and the CO molecules on Pt atoms.

The CO–O_2 and CO–NO reactions have been investigated in the presence of several surfaces of $Pt_{0.25}$–$Rh_{0.75}$ and $Pt_{0.10}$–$Rh_{0.90}$ single crystals (*45, 119, 142–144*). The results were compared with data for pure Pt and Rh surfaces to examine the effect of alloy formation. This comparison is of interest for understanding the synergistic effects reported by many groups for the CO oxidation catalyzed by supported Pt–Rh (*151–153*). Siera *et al.* (*142*) argued that beneficial effects of Pt–Rh alloy formation might be related to the strong preference of oxygen for the Rh sites on the surface. This effect might result in a better mixing of CO and O on the surface (with the O bound to Rh and CO adsorbed on Pt) and, hence, in a faster reaction at lower temperature. Similar effects might be expected for CO + NO (*142*) because CO has a slight preference for Pt and NO for Rh. However, Siera *et al.* (*45, 80, 142*) did not find any indication of a synergistic effect due to alloy formation. This result is consistent with those obtained in the same laboratory for supported Pt–Rh alloy catalysts (*80, 114, 150*).

Large differences were found by Siera *et al.* (*45*) in the steady-state reaction rates of both reactions catalyzed by four $Pt_{0.25}$–$Rh_{0.75}$ alloy surfaces in the low-pressure range. An example is shown in Fig. 25 for the NO + CO reaction and in Fig. 9 for the CO + O_2 reaction.
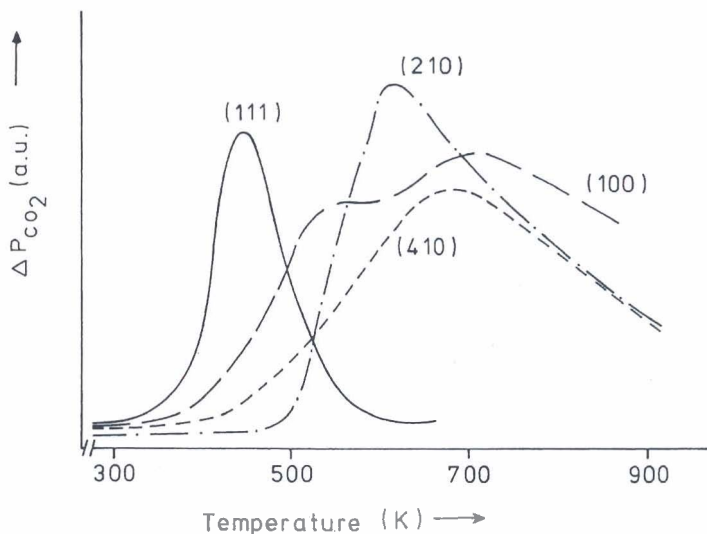
FIG. 25. Steady-state reaction rates of CO_2 production from CO + NO on Pt–Rh(111), (100), (410), and (210) under stoichiometric conditions [reproduced with permission from Siera *et al.* (*45*)].

This large effect of the surface structure is a remarkable observation for the CO + O_2 reaction since this reaction is usually considered to be a typical example of a reaction that is insensitive to the surface structure. The influence of the surface structure can be explained on the basis of the interaction of these surfaces with CO, NO, and O_2. A large CO inhibition occurs in the low temperature range (<400 K), especially for the CO + O_2 reaction. This effect is larger for the (210) surface than for the (111) surface due to the higher heat of adsorption of CO on the open (210) surface. The reaction order in CO becomes positive in the higher temperature range (550 K). A positive reaction order was found for oxygen in the whole temperature range, just as for pure Pt(111). However, for pure Rh(111) a negative reaction order in oxygen was found in the higher temperature range (*154*). This observation suggests that the Rh atoms in the Pt–Rh alloy are more difficult to oxidize in the presence of Pt atoms. Similar observations were made for the CO + NO reaction (*45*). In the low-temperature regime, the order in CO is negative. However, the reaction starts at significantly lower temperature, especially on the (111) surface, which is the least reactive surface for the N–O bond breaking. Hence, N–O dissociation is not the rate-determining step at low temperatures. For pure Rh(100) a reaction order of zero was reported by Oh *et al.* (*155*). Oh *et al.*

concluded that the Rh(100) surface is predominantly covered by NO. Pt–Rh alloy surfaces, on the other hand, are covered with both NO and CO at low temperatures. The CO molecules reside predominantly on the Pt atoms and the NO molecules on the Rh atoms in the alloy surface (150). Hence, it is likely that the Pt atoms in the alloy surface are covered with CO at low temperatures, causing the negative dependence of reaction rate on CO pressure.

Ng et al. (144) examined the NO–CO, CO–O_2, and CO–N_2O reactions on a $Pt_{0.10}$–$Rh_{0.90}$ (111) surface. The NO–CO activity of this alloy surface is similar to that of Rh(111) at temperatures from 573 to 648 K in that the two surfaces are represented by the same activation energy, reaction orders, and selectivity. The turnover frequencies are slightly lower than those for Rh(111) when compared on a per surface atom basis; however, the rates per surface Rh atom are virtually unchanged. The authors suggested that the primary effect of Pt is to dilute the Rh surface concentration.

Hirano et al. (78–80) investigated the reaction of NO with hydrogen on the (111), (100), and (410) surfaces of a $Pt_{0.25}$–$Rh_{0.75}$ single crystal and, for comparison, the pure Pt(100) and Rh(100) surfaces. Both the activity and the selectivity depend strongly on the surface structure and composition, as shown in Fig. 26.

In the low-temperature range ($\sim$ 520 K), the activity of the (100) surfaces decreases in the order Pt(100) > Pt–Rh(100) > Rh(100). The activity of pure Rh(100) is drastically enhanced by alloying with Pt. For the alloy surfaces, the order in activity at 520 K is (100) > (410) > (111). The order of intrinsic reactivity for NO bond breaking is Pt–Rh(410) > Rh(100) > Pt–Rh(100) > Pt(100) > Pt–Rh(111). Hence, these results indicate that NO bond scission is not the rate-determining step of the reaction. The selectivity toward N_2 decreases in the order Rh(100) $\sim$ Pt–Rh(410) > Pt(100) > Pt–Rh(111) at 520 K. It is well established that many vacant metal sites are required before NO dissociation can occur. If the surface is largely covered with molecularly adsorbed NO or with N adatoms, the reaction is inhibited by blocking of active sites. The conversion of NO at temperatures below 600 K is low for the Rh(100) surface due to the presence of strongly bound N atoms. The high selectivity of this surface is also caused by the high concentration of N adatoms. On Pt(100), the Pt–N bond strength is much weaker, resulting in a much lower concentration of N adatoms at 520 K. Free Pt sites remain available and, consequently, the reaction is fast but with a much lower selectivity toward N_2. The Pt–Rh(100) alloy surface shows a behavior intermediate between those of pure Pt and Rh(100).

The CO oxidation and NO reduction reactions have also been investigated in the presence of supported Pt–Rh catalysts. The results seem confusing: Whereas Oh and Carpenter (151) and Lyman et al. (153, 156) reported
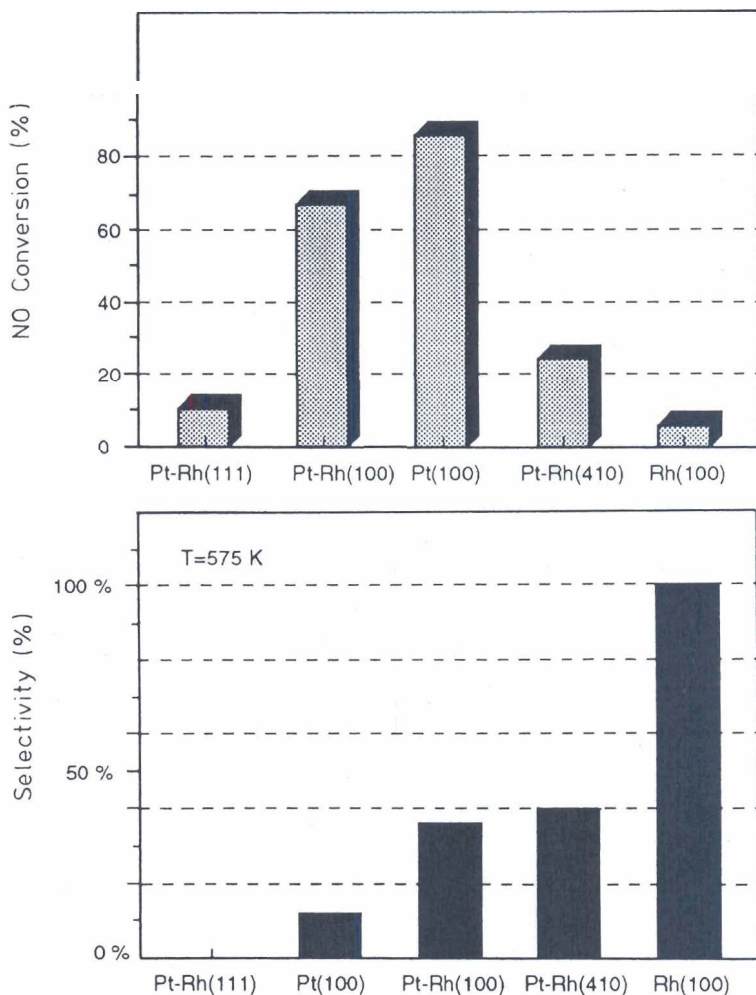
FIG. 26.   Relative activity (NO conversion after 3 min at 520 K) and selectivity for N_2 (at a conversion of 10%) for the reduction of NO by hydrogen on Pt, Rh, and Pt–Rh alloy single-crystal surfaces [reproduced with permission from Hirano *et al.* (*79*)].

a better performance of some bimetallic Pt–Rh/Al_2O_3 catalysts than those of individual Pt or Rh, results of other groups did not support the evidence for a synergistic effect (*80, 114, 157, 158*). For illustration, the results for the NO reduction reactions reported by Nieuwenhuys *et al.* (*80, 114, 157*) are summarized in Fig. 27, which shows the temperature required to achieve a constant turnover frequency versus the bulk catalyst composition. Both
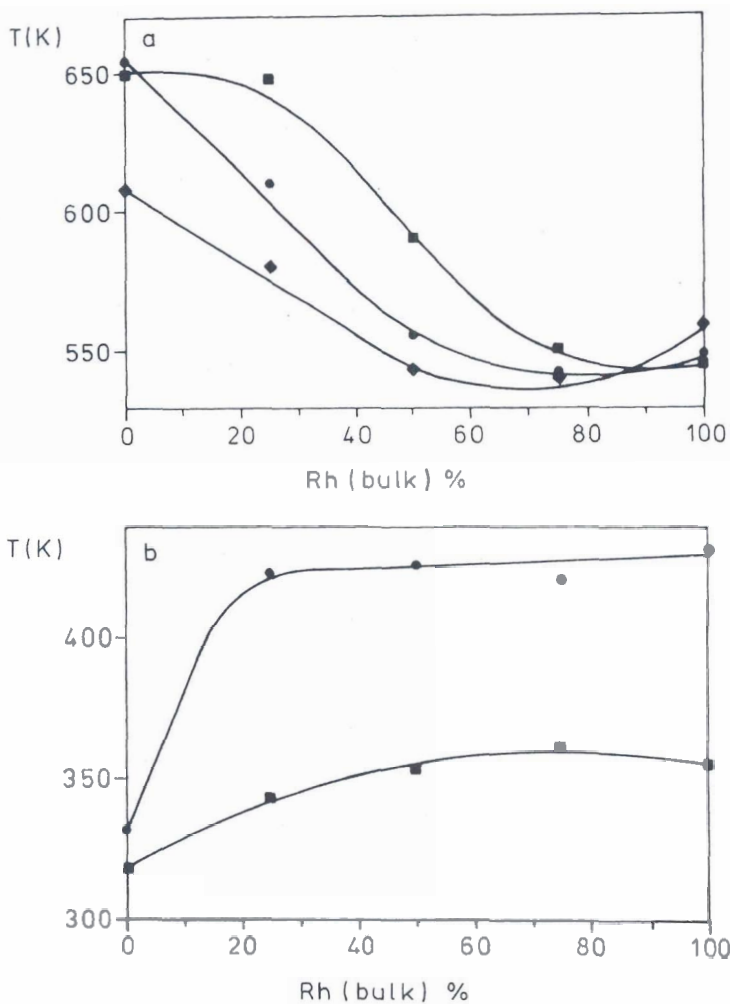
FIG. 27. (a) Temperature required for a constant turnover frequency of 0.05 s^{-1} for the NO + CO reaction on Pt–Rh on SiO$_2$ catalysts as a function of the bulk composition for three NO/CO ratios. ■, NO/CO = 1/4; ●, NO/CO = 1; ◆, NO/CO = 4. (b) Temperature required for a constant turnover frequency of 0.005 s^{-1} for the NO + H$_2$ reaction on Pt–Rh on SiO$_2$ catalysts as a function of the bulk composition for two NO/H$_2$ ratios. ●, NO/H$_2$ = 1; ■, NO/H$_2$ = 1/3 [reproduced with permission from Nieuwenhuys et al. (80)].

the activity and the selectivity of the Pt–Rh alloy catalysts are between those of the constituent metal catalysts. Rh/SiO$_2$ is more active in the NO + CO reaction than Pt/SiO$_2$. For this reaction the effect of changing feed composition is small for Rh and large for Pt. In uhv studies it was

also found that the reaction rate is a very weak function of the CO/NO ratio. For Pt/SiO$_2$ the results point to a significant CO inhibition, as has been observed under low-pressure conditions on Pt single-crystal surfaces. Only in a large excess of NO can a CO precovered Rh(100) surface be saturated with NO (*159*). On Rh the reaction occurs at temperatures much higher than the NO dissociation temperature. Apparently, the reaction rate is limited by the presence of N on the Rh catalyst. The NO + H$_2$ reaction starts at a much lower temperature on Pt/SiO$_2$ than on Rh/SiO$_2$, an observation that is consistent with the single-crystal work, discussed previously.

The catalytic performance of Pt–Rh alloys has been correlated with the surface composition expected on the basis of the single-crystal work (*80, 114*). The surface composition of Pt–Rh alloys varies strongly with conditions such as the gas composition. Clean Pt–Rh alloy surfaces are enriched with Pt. Adsorbates can easily induce segregation of Pt or Rh to the surface. Oxygen in the gas phase induces Rh surface segregation. For the NO + CO and NO + H$_2$ reactions, the activity of the Pt$_{0.5}$–Rh$_{0.5}$ alloy catalysts resembles that of pure Rh under net oxidizing conditions, whereas under net reducing conditions its activity is between those of Pt and Rh. This comparison suggests that the surface composition varies with the experimental conditions from almost pure Rh under net oxidizing conditions to, perhaps, a bulk-like or Pt-rich surface composition under net reducing conditions. However, the selectivity of this catalyst for the NO + H$_2$ reactions is different from those of both Pt and Rh. This comparison indicates that this catalyst contains Pt atoms in the surface that influence the selectivity. The activity of the Pt$_{0.75}$–Rh$_{0.25}$ alloy catalyst is almost equal to that of pure Pt under net reducing conditions, whereas its activity is between those of Pt and Rh under stoichiometric and net oxidizing conditions. Again, this comparison suggests that the surface composition changes with the feed composition. The properties of the Pt$_{0.25}$–Rh$_{0.75}$ alloy catalysts are notable. For both the NO + CO and NO + H$_2$ reactions the activity is equal to that of pure Rh under net oxidizing, stoichiometric, and net reducing conditions. Under net oxidizing conditions, a behavior such as that of pure Rh may indeed be expected. However, under net reducing conditions the presence of both Pt and Rh atoms should be expected on the surface. The relatively high activity of this catalyst for the NO + CO reaction might be caused by a beneficial effect of the presence of both Rh and Pt, i.e., the low CO inhibition on Rh sites and a beneficial effect of Pt on, for example, the amount of N or NO on the surface. For the NO + H$_2$ reaction, however, the presence of Pt atoms does not seem to diminish the inhibition effect of NO, probably because of the lower reaction temperatures.

The synergistic effect reported by Lyman *et al.* (*153, 156*) was found only for a Pt-rich catalyst with a very homogeneous composition of the particles.

Bimetallic catalysts with a bimodal particle composition distribution (Rh-rich and Pt-rich particles) did not show synergistic performance. Cai *et al.* (*153*) suggested that the absence of synergism in the observations of Nieuwenhuys *et al.* (*80, 114, 157*) may be attributed to the presence of bimodal particle composition distribution or to the low operating temperature regime used by Nieuwenhuys *et al.* due to the high activity of their catalysts. It is emphasized that the synergism observed by Cai *et al.* (*153*) is very small, smaller than 9 K expressed in terms of the temperature needed to achieve a conversion of 50%. In addition, the effect was not observed for the Pt–Rh catalysts with other compositions than 96% Pt, including a very Pt-rich $Pt_{0.99}$–$Rh_{0.01}$ catalyst. The synergistic effect found for the $Pt_{0.96}$–$Rh_{0.04}$ catalyst was explained by a beneficial effect of Pt on Rh reduction and by a higher probability of having both reactant species on neighboring sites.

In conclusion, the catalytic properties of supported Pt–Rh alloys are strongly dependent on the gas-phase composition, the bulk composition of the alloy particles, and the reaction temperature. A combination of factors determines the activities of the different catalysts. Under oxidizing conditions at sufficiently high temperatures, Rh segregation to the surface occurs. This is reflected in the catalytic activity of the Pt–Rh alloys which can vary between that of pure Pt and that of pure Rh. Large synergistic effects caused by alloying of Pt with Rh have not been observed. Differences in activity and selectivity for catalysts with different Pt–Rh compositions can be explained in terms of specific properties of the pure metals toward the adsorbates. Although most results show that the behavior of the alloy catalysts varies between those of Pt and Rh, care must be taken when interpreting the results in terms of absolute surface concentrations of Pt and Rh. The activity of an alloy catalyst depends on the surface composition of the metal particles. However, the relationship between activity, selectivity, and surface composition may be complicated for many reasons. The catalytic behavior varies with the concentration and the size of the various ensembles of atoms on the surface. All reaction steps (molecular adsorption, dissociation, and reaction between the species on the surface) may depend in different ways on the distribution of atoms over the surfaces. Furthermore, the small effect of alloying on the binding energies of adsorbed atoms and molecules may play a role in the catalytic performance of the alloys.

VI. Effects of the Additives Cerium and Lanthanum Oxides

It was noted in the introduction that the washcoat of the automobile catalysts contains several other oxides, mainly cerium and lanthanum oxide.

These rare earth oxides make an important contribution to catalyst perfor-
mance and durability and have multiple functions (160). The ceria content
of current three-way catalyst formulations is about 25 wt% (as cerium)
of the washcoat. Ceria was originally added to increase the stability and
dispersion of the noble metal (161). Ceria and, in particular, lathana are
thought to stabilize the γ-Al_2O_3 support by inhibiting its structure change
from the γ to the α modification (162–164). An important difference be-
tween the two rare earth oxides is the facile change of the oxidation state
of Ce, whereas La is valence invariant (La_2O_3) under operation conditions.
Cerium oxide can be partly reduced from CeO_2 to give oxygen-deficient
CeO_{2-x} (x is near one-half) and reoxidized to CeO_2 under oxidizing condi-
tions. Ceria is a chemically active component, as an oxygen buffer compo-
nent (165), as a promoter for the noble metal catalyst, and as a catalyst
for the water–gas shift reaction (166)

$$CO + H_2O \leftrightarrows CO_2 + H_2. \tag{35}$$

This reaction leads to an additional increase in CO conversion and to
the formation of hydrogen, which has a beneficial effect on NO reduction.
The oxygen storage capacity of ceria results in a widening of the effective
air/fuel ratio at which the reduction and oxidation reactions can operate
during the oscillatory cycle. Under fuel-rich (reducing) conditions, the
stored oxygen is released and is available for the oxidation of CO and hc;
oxygen is stored during fuel-lean (oxidizing) conditions, thereby enhancing
NO reduction to N_2.

Recently, direct promoter effects of ceria on the catalytic properties of
noble metals have been reported (167, 168). Addition of ceria to Rh/Al_2O_3
was found to improve NO reduction at low temperatures, with a decrease
in the apparent activation energy for the CO + NO reaction (168). A large
effect of the particle size of ceria was found for NO reduction catalyzed by
a $Pt/ceria/Al_2O_3$ (169). The authors proposed that the Pt–ceria interaction
increases by reduction of the ceria particle size. Although these promoter
effects of ceria on the noble metals are well documented, the origin of the
effects is not fully understood. The few surface science studies directed
at understanding these promoter effects provide some novel information.
Zafiris and Gorte (170) examined the structure and adsorption properties
of Pt and Rh deposited on amorphous ceria films. They reported that ceria-
supported Pt exhibits adsorption properties very similar to those of Al_2O_3-
supported Pt for CO, NO, and H_2. In contrast, large effects were found
for Rh on ceria; adsorption of CO and of NO is affected by ceria, and CO
adsorption results in a CO_2 formation peak during TDS. It was suggested
that O can migrate from ceria to the Rh surface at temperatures near
room temperature.

· Schmidt and Krause (*171*) and Schmidt and Schwartz (*172*) observed dramatic changes in the microstructures of Rh supported on thin films of SiO_2 and Al_2O_3 during heating in an atmosphere of NO, CO, or a mixture of NO + CO. Rh on silica is volatilized even by treatment in NO + CO at 570 K, but the addition of ceria retards this effect. Heating Rh on alumina in NO + CO had much less effect. However, heating in NO alone resulted in redispersion of Rh into small (20-Å) particles on the Al_2O_3. It was speculated that a mobile nitrosyl complex is formed during heating in NO, resulting in redispersion, and that volatilization occurs via formation of metal carbonyls.

Hardacre *et al.* (*173, 174*) investigated the properties, structure, and composition of cerium oxide films prepared by cerium deposition on Pt(111), finding that the activity for CO oxidation is enhanced on Pt(111) that is partially covered by ceria. It was suggested that new sites at the Pt–oxide interface become available for reaction. A remarkable observation is the high activity for CO oxidation when the Pt(111) sample is fully encapsulated by ceria (Pt was undetectable by XPS and AES). It was proposed that an ultrathin, disordered ceria film becomes the active catalyst. It was also demonstrated by XPS and AES that Pt dramatically increases the reducibility of cerium oxide that is in intimate contact with Pt. This result suggests that intimate contact between the noble metal and oxide phases is indeed crucial to facile oxygen release from ceria. High-resolution electron microscopy demonstrated the presence of direct contact between ceria and noble metal for supported Pt–Rh catalysts (*175*). Hardacre *et al.* (*173, 174*) related the catalytic activity of the ceria phase to partially reduced cerium oxide.

In conclusion, there is overwhelming evidence for the beneficial effect of cerium oxide on the activity of the noble metal catalyst. However, the nature of the "promoter" effect of ceria is not fully understood. Most likely, the noble metal–cerium oxide interface is of crucial importance for some of the effects observed. More studies with model systems are needed for a better understanding of the promoter effects of ceria.

VII.   Summary, Assessment, and Forecast

The automotive TWC is one of the major achievements of modern research in heterogeneous catalysis. There have been major efforts to elucidate the fundamental reaction pathways and the catalyst characteristics that account for the success of the TWC. The chemistry involved is understood in considerable detail as a result of work with idealized models of the TWC. The mechanisms of the CO oxidation and NO reduction reactions with

CO, hydrogen, and hc have been discussed in detail in this review. In particular, the application of various modern surface science techniques has advanced our understanding of the principles of the reactions on the atomic scale and the relationship of surface composition and structure to catalytic properties.

Surface science offers many opportunities in catalysis research because a variety of techniques are available to characterize in detail the composition and structure of the catalyst surface and to identify the adsorbed species. A frequent criticism of the surface science approach is that it is far removed from real catalysis since most of the surface science techniques can only be applied at low pressures and with "model" catalysts, often single-crystal surfaces. The so-called pressure gap has been bridged by combining, in the same apparatus, the techniques needed for surface analysis and character-ization with the ability to measure reaction rates at elevated pressures. In addition, many techniques can also be applied *in situ* at elevated pressures.

In this review, literature data concerning CO oxidation and NO reduction on model catalysts have been reviewed and compared with those reported for supported catalysts. The major differences in behavior of the three noble metals—Pt, Pd, and Rh—used in TWC have been assessed. It is concluded that the major mechanisms are reactions of the L–H type be-tween O_{ads}, CO_{ads}, and the dissociation products of NO, viz., N_{ads} and O_{ads}, with N_2 formed by combination of 2 N_{ads}, NH_3 by hydrogenation of N_{ads}, and N_2O by reaction between N_{ads} and NO_{ads}. Although other mechanisms have been proposed and their possible existence cannot be ruled out, the effects of the surface composition and structure, the specific differences in behavior of Pt, Pd, and Rh, the effect of changes in temperature, and variations in partial pressures can be fully understood on the basis of these reaction pathways.

The effects of alloy formation and the chemistry of the additive cerium oxide, although less well understood, have also been evaluated in detail. It was shown that the catalytic properties of Pt–Rh alloy catalysts are strongly dependent on the gas-phase composition and the bulk composition of the alloy particles. Many factors determine the activities of these catalysts. Under oxidizing conditions, Rh segregation to the surface occurs. This is reflected in the catalytic activity of the Pt–Rh alloys, which can vary between that of pure Pt and that of pure Rh. No large synergistic effects resulting from the alloying of Pt with Rh have been observed. The differences in activity observed for the different catalysts can be explained in terms of the specific properties of the pure metals toward the adsorbates. The activity and the selectivity of the Pt, Rh, and Pt–Rh surfaces depend on the surface structure and composition. The selectivity is determined by the relative concentrations of CO, NO, N, and H adsorbed on the various surfaces.

In fresh automotive exhaust catalysts, the precious metals are well distributed in the form of small crystallites with sizes between 0.5 and 5 nm. During aging, a severe loss of Pt surface area occurs due to sintering. Rh, however, remains in a highly dispersed state because it is partly in an oxidized state, whereas the Pt particles remain metallic. The morphology and composition of the catalyst particles change continuously during operation. Pt–Rh alloy particles are formed under reducing conditions. Under oxidizing conditions dealloying occurs, resulting in rhodium oxide particles being separated from metallic Pt and Pt–Rh alloy particles. During reaction, cerium switches between oxidation states leading to changes in the noble metal–Al_2O_3 (especially Rh) interactions. Ce-noble metal and Ce-support interactions can occur. Hence, a continuous restructuring and modification of catalytic behavior can occur. All these effects make the automotive TWC one of the most dynamic catalysts in use.

Interest in the control of emissions from automobiles will continue to grow because of increasingly stringent legislation worldwide for emission of hc, CO, NO_x, and particulates. Major new developments include (i) the introduction of a small catalytic converter, combined with the main converter containing the TWC, close to the engine manifold, enabling quicker light-off and therefore overall better CO and hc conversion and (ii) the development of catalytic converters for lean-burn gasoline-fueled engines and for diesel engines. Lean-burn versions of the four-stroke engine have been in development for many years. From the perspective of fuel economy and, hence, CO_2 emission, the use of lean-burn engines is desirable. The difficulty is in achieving NO_x conversion under such oxidizing conditions. The most thoroughly investigated catalysts are zeolites containing metal ions, in particular, Cu/ZSM5, Co/ZSM5, and other metal–zeolite systems. Unfortunately, these zeolites are deactivated at high temperatures in the presence of water (because of destruction of the zeolite structure), which is an inevitable component of automotive emissions. Although some reports suggest that many metal-containing zeolites, such as Fe/ZSM5 (*176, 177*) and cerium-exchanged mordenite (*178*), are stable in water vapor, it is not certain that a zeolite-based catalyst that meets the legislation standards for emission and catalyst lifetime will be developed. New technologies that are developing include NO_x catalysts that can reduce NO_x under oxidizing conditions, adsorbers/absorbers for NO_x and hc, particulate traps that are regenerated by catalytic oxidation using Pt, and novel catalysts that can convert CO immediately after the cold start.

REFERENCES

1. Taylor, K. C., *Catal. Sci. Technol.* **5**, 119 (1984).
2. Taylor, K. C., *Catal. Rev. Sci. Eng.* **35**, 457 (1993).

3. Shelef, M., and Graham, G. W., *Catal. Rev. Sci. Eng.* **36,** 433 (1994).
4. Bowker, M., and Joyner, R. W., *Insights Spec. Inorg. Chem.* 145 (1995).
5. Ramsier, R. D., and Yates, J. T., *Surf. Sci. Rep.* **12,** 243 (1991).
6. Winkler, A., and Rendulic, K. D., *Surf. Sci.* **118,** 19 (1982).
7. Nieuwenhuys, B. E., *Surf. Sci.* **126,** 307 (1983); *NATO-ASI Ser.* C **398,** 155 (1993) and references therein.
8. Gland, J. L., Sexton, B. A., and Fisher, G. B., *Surf. Sci.* **95,** 587 (1980).
9. Campuzano, J. P., *Chem. Phys. Solid State Surf. Sci. Catal.* **3A,** 389 (1991).
10. Blyholder, G., *J. Phys. Chem.* **68,** 2772 (1964).
11. Bagus, P. S., Nelin, C. J., and Bauschlicher, C. W., *J. Vac. Sci. Technol.* **A2,** 905 (1984).
12. Muller, W., and Bagus, P. S., *J. Vac. Sci. Technol.* **A3,** 1623 (1985).
13. Rangelov, G., Memmel, N., Bertel, E., and Dose, V., *Surf. Sci.* **251,** 965 (1991).
14. Nieuwenhuys, B. E., *Surf. Sci.* **105,** 505 (1981).
15. Eischens, R. P., Pliskin, W. A., and Francis, S. A., *J. Chem. Phys.* **22,** 1786 (1954).
16. Sheppard, N., and Nguyen, T. T., *in* "Advances in IR and Raman Spectroscopy" (R. E. Hester and R. J. H. Clark, Eds.), Vol. 5. Heyden, London, 1978.
17. Broden, G., Rhodin, T. N., Brucker, C., Bendow, R., and Hurych, Z., *Surf. Sci.* **59,** 593 (1976).
18. Benzinger, J. B., *Appl. Surf. Sci.* **6,** 105 (1980).
19. Gorodetski, V. V., and Nieuwenhuys B. E., *Surf. Sci.* **105,** 299 (1981).
20. Hendrickx, H. A. C. M., and Nieuwenhuys, B. E., *Surf. Sci.* **175,** 185 (1986).
21. Wolf, R. M., Bakker, J. W., and Nieuwenhuys B. E., *Surf. Sci.* **246,** 135 (1991).
22. van Hardeveld, R. M., Thesis, Technology University of Eindhoven, 1997.
23. Borg, H. J., Reijerse, J. F. C. J. M., van Santen, R. A., and Niemantsverdriet, J. W., *J. Chem. Phys.* **101,** 10051 (1994).
24. Sandell, A., Nilsson, A., and Martensson, N., *Surf. Sci.* **241,** L1 (1991).
25. Somorjai, G. A., *Surf. Sci.* **107,** 573 (1981).
26. Gorte, R. J., Schmidt, L. D., and Gland J. L., *Surf. Sci.* **109,** 367 (1981).
27. Masel, R. I., *Catal Rev.-Sci. Eng.* **28,** 335 (1986).
28. Janssen, N. M. H., Cholach, A. R., Ikai, M., Tanaka, K., and Nieuwenhuys, B. E., *Surf. Sci.* **382,** 201 (1997).
29. Solymosi, F., *J. Mol. Catal.* **65,** 337 (1991).
30. van Tol, M. F. H., Gielbert, A., Wolf, R. M., Lie, A. B. K., and Nieuwenhuys, B. E., *Surf. Sci.* **287/288,** 201 (1993).
31. Loffler, D. G., and Schmidt, L. D., *Surf. Sci.* **59,** 195 (1976).
32. Conrad, H., Ertl, G., and Küppers, J., *Surf. Sci.* **76,** 323 (1978).
33. Lambert, R. M., and Comrie, C. M., *Surf. Sci.* **46,** 61 (1974).
34. Thiel, P. A., Weinberg, W. H., and Yates, J. T., *J. Chem. Phys.* **71,** 1643 (1979).
35. King, D. A., *Faraday Disc. Chem. Soc.* **87,** 303 (1989).
36. van Slooten, R. F., and Nieuwenhuys, B. E., *J. Catal.* **122,** 429 (1990).
37. Gardner, S. D., Hofland, G. B., Upchurch, B. T., Schryer, D. R., Kielin, E. J., and Schryer, J., *J. Catal.* **129,** 114 (1991).
38. Ertl, G., *Adv. Catal.* **37,** 213 (1990).
39. Engel, T., and Ertl, G., *J. Chem. Phys.* **69,** 1267 (1978).
40. Campbell, C. I., Ertl, G., Kuipers, H., and Segner, J., *J. Chem. Phys.* **73,** 5862 (1980).
41. Gland, J. L., Sexton, B. A., and Fisher, G. B., *Surf. Sci.* **95,** 587 (1980).
42. Su, C. X., Cremer, P. S., Shen, Y. R., and Somorjai, G. A., *J. Am. Chem. Soc.* **119,** 3994 (1997).
43. Li, Y., Boecker, D., and Gonzalez, R. D., *J. Catal.* **110,** 319 (1988).

44. Wintterlin, J., Völkening, S., Janssens, T. V. W., Zambelli, T., and Ertl, G., *Science* **278,** 1931 (1997).
45. Siera, J., Rutten, F., and Nieuwenhuys, B. E., *Catal. Today* **10,** 353 (1991).
46. Cobden, P. D., Siera, J., and Nieuwenhuys, B. E., *J. Vac. Sci. Technol.* **A10,** 2487 (1992).
47. Sales, B. C., Turner, J. E., and Maple, M. B., *Surf. Sci.* **114,** 381 (1982).
48. Janssen, N. M. H., Cobden, P. D., and Nieuwenhuys, B. E., *J. Phys. Condens. Matters* **9,** 1889 (1997).
49. Imbihl, R., and Ertl, G., *Chem. Rev.* **95,** 697 (1995).
50. Mergler, Y. J., van Aalst, A., van Delft, J., and Nieuwenhuys, B. E., *Appl. Catal.* **B10,** 245 (1996).
51. Mergler, Y. J., and van Aalst, A., *ACS Symp. Ser.,* **587,** 196 (1995).
52. Mergler, Y. J., and Nieuwenhuys, B. E., *Appl. Catal.* **B12,** 95 (1997).
53. Mergler, Y. J., van Aalst A., van Delft, J., and Nieuwenhuys, B. E., *J. Catal.* **161,** 310 (1996).
54. Mergler, Y. J., Hoebink, J., and Nieuwenhuys, B. E., *J. Catal.* **167,** 305 (1997).
55. Matsushima T., *Surf. Sci.* **127,** 403 (1983).
56. Wintterlin, J., Schuster, R., and Ertl, G., *Phys. Rev. Lett.* **77,** 123 (1996).
57. Brune, H., Wintterlin, J., Trost, J., Ertl, G., Weichers, J., and Behm, R. J., *J. Chem. Phys.* **99,** 2128 (1993).
58. Fadeev, E., Gorodetskii, V., and Smirnov, M., *in* "Proceedings of the Boreskov Memorial Symposium" (1997) Novosibirsk, Russia.
59. Watanabe, K., Uetsuka, H., Ohnuma, H., and Kunimori, K., *Catal. Lett.* **47,** 17 (1997).
60. Mullins, C. B., Rettner, C. T., and Auerbach, D. J., *J. Chem. Phys.* **95,** 8649 (1991).
61. Wartnaby, C. E., Stuck, A., Yeo, Y. Y., and King, D. A., *J. Chem. Phys.* **102,** 1855 (1995).
62. Boudart, M., *J. Mol. Catal. A* **120,** 271 (1997) (and references therein).
63. Szanyi, J., and Goodman, D. W., *J. Phys. Chem.* **98,** 2972 (1994).
64. Szanyi, J., Kuhn, W. K., and Goodman, D. W., *J. Phys. Chem.* **98,** 2978 (1994).
65. Peden, C. H. F., *ACS Symp. Ser.* **482,** 143 (1992).
66. Peden, CH. F., Goodman, D. W., Blair, D. S., Berlowitz, P. J., Fisher, G. B., and Oh, S. H., *J. Phys. Chem.* **92,** 1563 (1988).
67. Oh, S. H., Fisher, G. B., Carpenter, J. E., and Goodman, D. W., *J. Catal.* **100,** 360 (1986).
68. Su, X., Jensen, J., Yang, M. X., Sameron, M. B., Shen, Y. R., and Somorjai, G. A., *Faraday Disc.* **105,** 263 (1996).
69. Bowker, M., Guo, Q., and Joyner, R. W., *Catal. Lett.* **18,** 119 (1993).
70. Kruse, N., and Gaussmann, A., *Surf. Sci.* **266,** 51 (1992).
71. Schwartz, S. B., Fisher, G. B., and Schmidt, L. D., *J. Phys. Chem.* **92,** 389 (1988).
72. van den Brink, P. J., and McDonald, C. R., SAE Tech. Paper No. 952399 (1995); *Appl. Catal. B* **6,** L97 (1995).
73. Kobylinski, T. P., and Taylor, B. W., *J. Catal.* **33,** 376 (1974).
74. Solymosi, F., Völgyesi, L., and Sárkány, J., *J. Catal.* **53,** 336 (1978).
75. Bamwenda, G. R., Obuchi, A., Ogata, A., and Mizuno, K., *Chem. Lett.* **2109,** (1994).
76. van Hardeveld, R. M., Schmidt, A. J. G. W., van Santen, R. A., and Niemantsverdriet, J. W., *J. Vac. Sci. Technol.* **A15,** 1558 (1997).
77. Chin, A., and Bell, A. T., *J. Phys. Chem.* **87,** 3700 (1983).
78. Hirano, H., Yamada, T., Tanaka, K., Siera, J., Cobden, P. D., and Nieuwenhuys, B. E., *Surf. Sci.* **262,** 97 (1992).
79. Hirano, H., Yamada, T., Tanaka, K., Siera, J., and Nieuwenhuys, B. E., *Stud. Surf. Sci. Catal.* **75,** 345 (1993).
80. Nieuwenhuys, B. E., Siera, J., Tanaka, K., and Hirano, H., *ACS Symp. Ser.* **552,** 114 (1994).
81. Yamada, T., and Tanaka, K., *J. Am. Chem. Soc.* **113,** 1173 (1991).

82. Zemlyanov, D. Y., Smirnov, M. Y., Gorodetskii, V. V., Block, J. H., *Surf. Sci.* **329**, 61 (1995).
83. Zemlyanov, D. Y., Smirnov, M. Y., and Gorodetskii, V. V., *Surf. Sci.,* in press.
84. Sun, Y. M., Sloan, S., Ihm, H., and White, J. M., *J. Vac. Sci. Technol.* **A14**, 1516 (1996).
85. van Hardeveld, R. M., van Santen, R. A., and Niemantsverdriet, J. W., *J. Phys. Chem.* **101**, 998 (1997).
86. Dietrich, H., Jacobi, K., and Ertl, G., *Surf. Sci.* **377–379**, 308 (1997); *J. Chem. Phys.* **106**, 9313 (1997).
87. Williams, C. T., Tolia, A. A., Weaver, M. J., and Takoudis, C. G., *Chem. Eng. Sci.* **51**, 1673 (1996).
88. Tolia, A. A., Williams, C. T., Takoudis, C. G., and Weaver, M. J., *J. Phys. Chem.* **99**, 4599 (1995).
89. Hecker, W. C., and Bell, A. T., *J. Catal.* **92**, 247 (1985).
90. Kiskinova, M., Lizzit, S., Comelli, G., Paolucci, G., and Rosei, R., *Appl. Surf. Sci.* **64**, 185 (1993).
91. Cobden, P. D., Nieuwenhuys, B. E., Esch, F., Baraldi, A., Comelli, G., Lizzit, S., and Kiskinova, M, *J. Vac. Technol. A*, **16**, 1014 (1999).
92. Klein, R. L., Schwartz, S., and Schmidt, L. D., *J. Phys. Chem.* **89**, 4908 (1985).
93. Lesley, M. W., and Schmidt, L. D., *Surf. Sci.* **155**, 215 (1985).
94. Li, Y., Slager, T. L., and Armor, J. N., *J. Catal.* **150**, 388 (1994).
95. Witzel, F., Sill, G. A., and Hall, W. K., *J. Catal.* **149**, 229 (1994).
96. Adelman, B. J., Beutel, T., Lei, G. D., and Sachtler, W. M. H., *Appl. Catal.* **B11**, L1 (1996).
97. Salama, T. M., Ohnishi, R., and Ichikawa, M., *Chem. Commun.* **105**, (1997).
98. Otto, K., Shelef, M., and Kummer, J. T., *J. Phys. Chem.* **74**, 2690 (1970).
99. Xu, H., and Ng, K. Y. S., *Appl. Phys. Lett.* **68**, 496 (1996); *Surf. Sci.* **365**, 779 (1996).
100. Leibsle, F. M., Murray, P. W., Francis, S. M., Thornton, G. T., and Bowker, M., *Nature* **363**, 706 (1993).
101. Hecker, W. C., and Bell, A. T., *J. Catal.* **84**, 200 (1983); **85**, 389 (1984).
102. Belton, D. N., and Schmieg, S. J., *J. Catal.* **144**, 9 (1993); **138**, 70 (1992).
103. Belton, D. N., DiMaggio, C. L., Schmieg, S. J., and Ng, K. Y. S., *J. Catal.* **157**, 559 (1995).
104. Makeev, A. G., and Slinko, M. M., *Surf. Sci.* **359**, L467 (1996).
105. Bugyi, L., and Solymosi, F., *Surf. Sci.* **188**, 475 (1987).
106. Root, T. W., Schmidt, L. D., and Fisher, G. B., *Surf. Sci.* **134**, 30 (1983).
107. Permana, H., Ng, K. Y. S., Peden, C. H. F., Schmieg, S. J., Lambert, D. K., and Belton, D. N., *J. Catal.* **164**, 194 (1996).
108. Zhdanov, V. P., and Kasemo, B., *Surf. Sci. Rep.* **29**, 31 (1997).
109. Ikai, M., He, H., Borroni-Bird, C. E., Hirano, H., and Tanaka, K., *Surf. Sci.* **315**, L973 (1994).
110. Ikai, M., and Tanaka, K., *Surf. Sci.* **357/358**, 781 (1996).
111. Ikai, M., Thesis, University of Tokyo, 1996.
112. Rainer, D. R., Vesecky, S. M., Koranne, M., Oh, W. S., and Goodman, D. W., *J. Catal.* **167**, 234 (1997).
113. Kummer, J. T., *J. Phys. Chem.* **90**, 4747 (1986).
114. Wolf, R. M., Siera, J., van Delft, F. C. M. J. M., and Nieuwenhuys, B. E., *Faraday Disc. Chem. Soc.* **87**, 275 (1989).
115. van Delft, F. C. M. J. M., Nieuwenhuys, B. E., Siera, J., and Wolf, R. M., *Iron Steel Inst. Jpn. Int.* **29**, 550 (1989).
116. Nieuwenhuys, B. E., *Surf. Rev. Lett.* **3**, 1869 (1996).
117. Kim, S., and d'Aniello, M. J., Jr., *Appl. Catal.* **56**, 23, 45 (1989).

118. Maire, F., Capelle, M., Meunier, G., Beziau, J. F., Bazin, D., Dexpert, H., Garin, F., Schmitt, J. L., and Maire, G., *Stud. Surf. Sci. Catal.* **96,** 749 (1995).
119. Nieuwenhuys, B. E., *in* "The Chemical Physics of Solid Surfaces" (D. A. King and D. P. Woodruff, Eds.), Vol. 6, p. 185. Elsevier, Amsterdam, 1993.
120. Kuijers, F. J., Tieman, B., and Ponec, V., *Surf. Sci.* **75,** 657 (1978).
121. Batirev, I. G., and Leiro, J. A., *J. Electr. Spectr. Rel. Phen.* **71,** 79 (1995).
122. Siera, J., van Delft, F. C. M. J. M., van Langeveld, A. D., and Nieuwenhuys, B. E., *Surf. Sci.* **264,** 435 (1992).
123. Tsong, T. T., *Surf. Sci. Rep.* **8,** 127 (1988).
124. Beck, D. D., DiMaggio, C. L., and Fisher, G. B., *Surf. Sci.* **297,** 293, 303 (1993).
125. Altenstaedt, W., and Leisch, M., *Appl. Surf. Sci.* **94/95,** 403 (1996).
126. LeGrand, B., and Treglia, G., *Surf. Sci.* **236,** 398 (1990).
127. Schoeb, A. M., Raeker, T. J., Yang, L., Wu, X., King, T. S., and De Pristo, A. E., *Surf. Sci. Lett.* **278,** L125 (1992).
128. Matsumoto, Y., Okawa, Y., Fujita, T., and Tanaka K., *Surf. Sci.* **355,** 109 (1996).
129. Wouda, P. T., Nieuwenhuys, B. E., Schmid, M., and Varga, P., *Surf. Sci.* **359,** 310 (1996).
130. Matsumoto, Y., Aibara, Y., Mukai, K., Moriwaki, K., Okawa, Y., Nieuwenhuys, B. E., and Tanaka, K., *Surf. Sci.* **377–379,** 32 (1997).
131. Wouda, P. T., Schmid, M., Hebenstreit, W., and Varga, P., *Surf. Sci.* **388,** 63 (1997).
132. Zhu, Y., and Schmidt, L., *Surf. Sci.* **129,** 107 (1983).
133. Wang, T., and Schmidt, L., *J. Catal.* **70,** 187 (1981).
134. Chen, M., and Schmidt, L., *J. Catal.* **56,** 198 (1979).
135. Graham, G. W., Potter, T., Baird, R. J., Ghandi, H. S., and Shelef, M., *J. Vac. Sci. Technol.* **A4,** 1613 (1986).
136. Wang, Z., Ansermet, J. P., Slichter, C. P., and Sinfelt J. H., *J. Chem. Soc. Faraday Trans I* **84,** 3785 (1988).
137. Savargaonkar, N., Khanra, B. C., Pruski, M., and King, T. S., *J. Catal.* **162,** 277 (1996).
138. Gorodetski, V. V., Nieuwenhuys, B. E., Sachtler, W. M. H., and Boreskov, G. K., *Surf. Sci.* **108,** 225 (1981).
139. Yamada, T., Hirano, H., Tanaka, K., Siera, J., and Nieuwenhuys, B. E., *Surf. Sci.* **226,** 1 (1990).
140. Tanaka, K. I., Yamada, T., and Nieuwenhuys, B. E., *Surf. Sci.* **242,** 503 (1991).
141. Siera, J., Koster van Groos, M. J., and Nieuwenhuys, B. E., *Recl. Trav. Chim. Pays–Bas.* **109,** 127 (1990).
142. Siera, J., van Silfhout, R., Rutten, F. J. M., and Nieuwenhuys, B. E., *Stud. Surf. Sci. Catal.* **71,** 395 (1991).
143. Fisher, G. B., Dimaggio, C. L., and Beck, D. D., *Stud. Surf. Sci. Catal.* **75,** 383 (1993).
144. Ng, K. Y. S., Belton, D. N., Schmieg, S. J., and Fisher, G. B., *J. Catal.* **146,** 394 (1994).
145. Rutten, F. J. M., Nieuwenhuys, B. E., McCoustra, M. R. S., Hollins, P., and Chesters, M. A., *J. Vac. Sci. Technol.* **A15,** 11619 (1997).
146. Taniguchi, M., Kuzembaev, E. K., and Tanaka, K., *Surf. Sci.* **290,** L711 (1993).
147. Tamura, H., Sasahara, A., and Tanaka, K., *Surf. Sci.* **303,** L379 (1994).
148. Gorte, R. J., and Schmidt, L. D., *Surf. Sci.* **111,** 260 (1981).
149. Sasahara, A., Tamura, H., and Tanaka, K., *Catal. Lett.* **28,** 161 (1994); *J. Phys. Chem.* **100,** 15229 (1996); *J. Phys. Chem. B* **101,** 1186 (1997).
150. Heezen, L., Kilian, V. N., van Slooten, R. F., Wolf, R. M., and Nieuwenhuys, B. E., *Stud. Surf. Sci. Catal.* **71,** 381 (1991).
151. Oh, S. H., and Carpenter, J. E., *J. Catal.* **98,** 178 (1986).
152. Tzou, M. S., Asakura, K., Yamazaki, Y., and Kuroda, H., *Catal. Lett.* **11,** 33 (1991).
153. Cai, Y., Stenger, H. G., Jr., and Lyman, C. E., *J. Catal.* **161,** 123 (1996).

154. Schwartz, S. B., Schmidt, L. D., and Fisher, G. B., *J. Phys. Chem.* **90,** 6194 (1986).
155. Oh, S. H., Fisher, G. B., Carpenter, J. E., and Goodman, D. W., *J. Catal.* **100,** 360 (1986).
156. Lakis, L. E., Cai, Y., Stengerrand, H. G., and Lyman, C. E., *J. Catal.* **154,** 276 (1995).
157. van den Bosch-Driebergen, A. G., Kieboom, M. N. H., van Dreumel, A., Wolf, R. M., van Delft, C. M. J. M., and Nieuwenhuys, B. E., *Catal. Lett.* **2,** 83, 235 (1989).
158. Anderson, J. A., *J. Catal.* **142,** 153 (1993).
159. Schwartz, S. B., and Schmidt, L. D., *Surf. Sci.* **206,** 169 (1988).
160. Harrison, B., Diwell, A. F., and Hallett, C., *Plat. Met. Rev.* **32,** 73 (1988).
161. Summers, J. C., and Ausen, S. A., *J. Catal.* **58,** 131 (1979).
162. Ozawa, M., and Kimura, M., *J. Mater. Sci. Lett.* **291** (1990).
163. Bettman, M., Chase, R. E., Otto, K., and Weber, W. H., *J. Catal.* **117,** 447 (1989).
164. Oudet, F., Courtine, P., and Vejux, A., *J. Catal.* **114,** 112 (1988).
165. Yao, H. C., and Yao, Y. F. J., *J. Catal.* **86,** 254 (1984).
166. Kim, G., *Ind. Eng. Chem. Prod. Res. Dev.* **21,** 267 (1982).
167. Loof, P., Kasemo, B., Anderson, S., and Frestad, A., *J. Catal.* **130,** 181 (1991).
168. Oh, S. H., *J. Catal.* **124,** 477 (1990).
169. Nunan, J. G., Robota, H. J., Cohn, M. J., and Bradley, S. H., *J. Catal.* **133,** 309 (1992).
170. Zafiris, G. S., and Gorte, R. J., *Surf. Sci.* **276,** 86 (1992); *J. Catal.* **139,** 561 (1993).
171. Krause, R. S., and Schmidt, L. D., *J. Catal.* **140,** 424 (1993).
172. Schwartz, J. M., and Schmidt, L. D., *J. Catal.* **148,** 22 (1994).
173. Hardacre, C., Ormerod, R. M., and Lambert, R. M., *J. Phys. Chem.* **98,** 10901 (1994).
174. Hardacre, C., Roe, G. M., and Lambert, R. M., *Surf. Sci.* **326,** 1 (1995).
175. Benaissa, M., Pham-Huu, C., Werckman, J., Crouzet, C., and Ledoux, M. J., *Catal. Today* **23,** 263 (1995).
176. Feng, X., and Hall, W. K., *J. Catal.* **166,** 368 (1997).
177. Chen, H., and Sachtler, W. M. H., *Catal. Today,* **42,** 73 (1998).
178. Ito, E., Mergler, Y. J., Nieuwenhuys, B. E., Calis, H. P. A., van Bekkum, H., and van der Bleek, C. M., *J. Chem. Soc. Faraday Trans.* **92,** 1799 (1996).